



NAVAL POSTGRADUATE SCHOOL

MONTEREY, CALIFORNIA

THESIS

**DYNAMICAL INFLUENCE AND OPERATIONAL
IMPACTS OF AN EXTREME MEDITERRANEAN COLD
SURGE**

by

Adam Shinabarger

June 2013

Thesis Co-Advisors:

Patrick Harr
Richard Moore

Approved for public release; distribution is unlimited

THIS PAGE INTENTIONALLY LEFT BLANK

REPORT DOCUMENTATION PAGE			Form Approved OMB No. 0704-0188	
Public reporting burden for this collection of information is estimated to average 1 hour per response, including the time for reviewing instruction, searching existing data sources, gathering and maintaining the data needed, and completing and reviewing the collection of information. Send comments regarding this burden estimate or any other aspect of this collection of information, including suggestions for reducing this burden, to Washington headquarters Services, Directorate for Information Operations and Reports, 1215 Jefferson Davis Highway, Suite 1204, Arlington, VA 22202-4302, and to the Office of Management and Budget, Paperwork Reduction Project (0704-0188) Washington DC 20503.				
1. AGENCY USE ONLY (Leave blank)		2. REPORT DATE June 2013	3. REPORT TYPE AND DATES COVERED Master's Thesis	
4. TITLE AND SUBTITLE DYNAMICAL INFLUENCE AND OPERATIONAL IMPACTS OF AN EXTREME MEDITERRANEAN COLD SURGE			5. FUNDING NUMBERS	
6. AUTHOR(S) Adam Shinabarger				
7. PERFORMING ORGANIZATION NAME(S) AND ADDRESS(ES) Naval Postgraduate School Monterey, CA 93943-5000			8. PERFORMING ORGANIZATION REPORT NUMBER	
9. SPONSORING /MONITORING AGENCY NAME(S) AND ADDRESS(ES) N/A			10. SPONSORING/MONITORING AGENCY REPORT NUMBER	
11. SUPPLEMENTARY NOTES The views expressed in this thesis are those of the author and do not reflect the official policy or position of the Department of Defense or the U.S. government. IRB Protocol number ____N/A____.				
12a. DISTRIBUTION / AVAILABILITY STATEMENT Approved for public release;distribution is unlimited			12b. DISTRIBUTION CODE A	
13. ABSTRACT (maximum 200 words) In February 2004, a significant cold surge from eastern Europe extended southward over the Aegean Sea and as far south as the northern coasts of Egypt and Libya. The system examined in this study caused over 45 cm of snowfall in Souda Bay, Crete, which significantly impacted operations at Naval Support Activity Souda Bay. The extratropical wave associated with the cold surge could be classified as a classic life-cycle 1 wave break. The wave-breaking event is linked to successive cyclogenesis over the western North Atlantic and a significant ridge-building event over the eastern North Atlantic. This case study will examine the role of dynamic processes that include the warm conveyor belts of the midlatitude cyclones and the warm-air advection that led the ridge over the North Atlantic. The significance of the ridge-trough couplet with respect to climatology is examined. Ensemble forecasts are used to examine the predictability of the cold surge event and its dependence on the upstream synoptic scale events.				
14. SUBJECT TERMS Extratropical Cyclone, Souda Bay, Crete, Genoa Low, Cold Surge, Rossby Wave Break, Dynamic Tropopause, Potential Vorticity			15. NUMBER OF PAGES 77	
			16. PRICE CODE	
17. SECURITY CLASSIFICATION OF REPORT Unclassified	18. SECURITY CLASSIFICATION OF THIS PAGE Unclassified	19. SECURITY CLASSIFICATION OF ABSTRACT Unclassified	20. LIMITATION OF ABSTRACT UU	

THIS PAGE INTENTIONALLY LEFT BLANK

Approved for public release; distribution is unlimited

**DYNAMICAL INFLUENCE AND OPERATIONAL IMPACTS OF AN EXTREME
MEDITERRANEAN COLD SURGE**

Adam Shinabarger
Lieutenant Commander, United States Navy
B.S. Michigan State University, 2002

Submitted in partial fulfillment of the
requirements for the degree of

**MASTER OF SCIENCE IN METEOROLOGY AND PHYSICAL
OCEANOGRAPHY**

from the

**NAVAL POSTGRADUATE SCHOOL
June 2013**

Author: Adam Shinabarger

Approved by: Patrick Harr
Thesis Co-Advisor

Richard Moore
Thesis Co-Advisor

Wendell A. Nuss
Chair, Department of Meteorology and Physical
Oceanography

THIS PAGE INTENTIONALLY LEFT BLANK

ABSTRACT

In February 2004, a significant cold surge from eastern Europe extended southward over the Aegean Sea and as far south as the northern coasts of Egypt and Libya. The system examined in this study caused over 45 cm of snowfall in Souda Bay, Crete, which significantly impacted operations at Naval Support Activity Souda Bay. The extratropical wave associated with the cold surge could be classified as a classic life-cycle 1 wave break. The wave-breaking event is linked to successive cyclogenesis over the western North Atlantic and a significant ridge-building event over the eastern North Atlantic. This case study will examine the role of dynamic processes that include the warm conveyor belts of the midlatitude cyclones and the warm-air advection that led the ridge over the North Atlantic. The significance of the ridge-trough couplet with respect to climatology is examined. Ensemble forecasts are used to examine the predictability of the cold surge event and its dependence on the upstream synoptic scale events.

THIS PAGE INTENTIONALLY LEFT BLANK

TABLE OF CONTENTS

I.	INTRODUCTION.....	1
A.	MOTIVATION.....	1
1.	Cold Surge and Snowfall Event over Crete	1
2.	Timeline	2
3.	Ingredients for Development of the Extreme Cold Surge	3
a.	<i>Cyclone Development</i>	3
b.	<i>Ridge Amplification</i>	4
4.	Predictability	4
B.	OBJECTIVE	5
II.	BACKGROUND.....	7
A.	BAROCLINIC LIFE CYCLE CHARACTERISTICS	7
B.	WARM CONVEYOR BELT AND RIDGE BUILDING.....	10
C.	ENSEMBLE FORECASTING	13
III.	METHODOLOGY.....	15
A.	DATA	15
1.	Analysis Data	15
2.	Satellite Imagery	15
B.	PREDICTABILITY.....	15
C.	DYNAMIC TROPOPAUSE.....	16
D.	STANDARDIZED ANOMALIES.....	17
IV.	ANALYSIS AND RESULTS.....	19
A.	PRECURSOR EVOLUTION: FEBRUARY 6-11 2004.....	19
B.	WAVEBREAK AND COLD SURGE	29
C.	PREDICTABILITY.....	36
V.	CONCLUSIONS AND RECOMMENDATIONS.....	51
A.	SYNOPTIC DEVELOPMENT	51
B.	PREDICTABILITY.....	52
C.	RECOMMENDATIONS	52
	LIST OF REFERENCES.....	55
	INITIAL DISTRIBUTION LIST	57

THIS PAGE INTENTIONALLY LEFT BLANK

LIST OF FIGURES

Figure 1.	Navy personnel clearing snow from a gate at Naval Support Activity Souda Bay and airfield, 13 February 2004 (From U.S. Navy archives).....	1
Figure 2.	Timeline of synoptic weather events between 5–13 February 2004.....	3
Figure 3.	Eddy kinetic energy evolution for LC1 (dashed) and LC2 (solid). Day 0 is defined as the introduction of the small pressure perturbation into the mean zonal flow (From Thorncroft et al., 1993).	9
Figure 4.	Schematic depicting (a) an initial perturbation before meridional wind shear has tilted the flow. The dashed line represents the flow after deformation from (b) anticyclonic tilting associated with an LC1 and (c) cyclonic tilting associated with an LC2 (From Thorncroft et al., 1993).	9
Figure 5.	Schematic of atmospheric conveyor belts. The WCB is depicted in orange (From University Corporation for Atmospheric Research).....	10
Figure 6.	Seasonal mean spatial distribution of (a), WCB starting points and (e) WCB trajectory positions after (b) and (f) 24-h, (c) and (g) 48-h, (d) and (h) 72-h for (a)–(d) June-July-August and (e)–(g) December-January-February. Depicted is the fraction (in percent) of all trajectories that fulfill the WCB criteria, averaged over 15 years. Different color scales were used for different days for clarity. The red boxes in (a) used for additional analysis not shown here (From Eckhardt et al., 2004).....	11
Figure 7.	Depiction of the evolution of the dynamic tropopause (a) under the influence of an upper-level trough and positive potential vorticity anomaly and (b) subsequent downstream effects of mid-level diabatic heating on the PV tendency.	12
Figure 8.	Surface temperature anomalies over 24 hours in degrees Kelvin over Europe for (a) 11 February, (b) 12 February, (c) 13 February, and (d) 14 February. Image created using the Earth System Research Laboratory Physical Sciences Division website (http://www.esrl.noaa.gov/psd/data/composites/day/).	20
Figure 9.	Timeline of synoptic weather events 5–13 February 2004 with emphasis on ridge amplification in the north Atlantic 6–10 February.	21
Figure 10.	Potential temperature and winds on the dynamic tropopause (DT) at (a) 0000 UTC 6 February, (b) 0000 UTC 7 February, (c) 0000 8 February, (d) 0000 UTC 9 February, and (e) 0000 UTC 10 February. 10e also defines the WCB at 0000 UTC 10 February. The DT is defined as the 2.0 PVU surface. Potential temperature (K) on the DT is defined by the shading. Winds on the DT are defined by the barbs, and one large barb is defined as 5 m s^{-1} . Layer-averaged relative vorticity between 925 and 850 hPa is	

	defined by the solid black contours. The L's define the circulation center of the three cyclones at the surface.....	23
Figure 11.	Tracks of three midlatitude cyclones defined in Figures 10a–10e. The circle size represents minimum sea-level pressure for the date time. Color coding defines the date.	26
Figure 12.	Water vapor satellite image from GOES 12 for 1800 UTC 7 February. The red line defines the WCB associated with L2.....	26
Figure 13.	Depiction of ridge amplification over central North Atlantic as defined by the 5340 m and 5460 m 1000–500 hPa thickness. Tracks of cyclones identified in Figures 10a–10e are defined by the solid black lines. Color coding defines the dates.	27
Figure 14.	The 1800 UTC 10 February 300 hPa heights (dam, black lines) and standardized anomalies (shading) defined as standard.	28
Figure 15.	The 1800 UTC 10 February 500 hPa heights (dam, black lines) and standardized anomalies (shading) defined as standard deviations. ...	28
Figure 16.	The 1800 UTC 10 February 925 hPa heights (dam, black lines) and standardized anomalies (shading) defined as standard deviations. ...	29
Figure 17.	Timeline of synoptic weather events 5–13 February 2004 with emphasis on the anticyclonic wavebreak over Europe 11–12 February.....	29
Figure 18.	As in Figure 10a, except for (a) 1200 UTC 11 February, (b) 1200 UTC 12 February, and (c) 1200 UTC 13 February	31
Figure 19.	The 1200 UTC 13 February 300 hPa heights (dam, black lines) and standardized anomalies (shading) defined as standard deviations. ...	33
Figure 20.	The 1200 UTC 13 February 500 hPa heights (dam, black lines) and standardized anomalies (shading) defined as standard deviations. ...	33
Figure 21.	The 1200 UTC 13 February 925 hPa heights (dam, black lines) and standardized anomalies (shading) defined as standard deviations	34
Figure 22.	Vertical cross section for 0000 UTC 13 February with end points A and B defined by the inset map. The solid black line defines the tropopause, the long wind barbs define 5 m s^{-1} , flags define 25 m s^{-1} , shading defines potential vorticity in PVU, and the dashed black define ascent in $10^{-4} \text{ hPa s}^{-1}$. Souda Bay is located at 24°E longitude.....	35
Figure 23.	Vertical cross section for 1200 UTC 13 February with end points A and B defined by the inset map. The solid black line defines the tropopause, the wind barbs define 5 m s^{-1} , flags define 25 m s^{-1} , shading defines potential vorticity in PVU, and the dashed black define ascent in $10^{-4} \text{ hPa s}^{-1}$. Souda Bay is located at 24°E longitude.....	36
Figure 24.	The 0000 UTC 11 February analyzed 500 hPa ensemble-mean heights, and the (b) 72-h, (c) 96-h, and (d) 120-h ensemble-mean forecasts of 500 hPa heights (black contours in dam). Shading represents standard deviation (m) about the ensemble.....	37

Figure 25.	The 0000 UTC 12 February analyzed 500 hPa ensemble-mean heights, and the (b) 72-h, (c) 96-h, and (d) 120-h ensemble-mean forecasts of 500 hPa heights (black contours in dam). Shading represents standard deviation (m) about the ensemble.....	38
Figure 26.	The 0000 UTC 13 February analyzed 500 hPa ensemble-mean heights, and the (b) 72-h, (c) 96-h, and (d) 120-h ensemble-mean forecasts of 500 hPa heights (black contours in dam). Shading represents standard deviation (m) about the ensemble.....	39
Figure 27.	The 0000 UTC 11 February analyzed SLP ensemble-mean heights, and the (b) 72-h, (c) 96-h, and (d) 120-h ensemble-mean forecasts of SLP (black contours in hPa). Shading represents standard deviation (hPa) about the ensemble.	40
Figure 28.	The 0000 UTC 12 February analyzed SLP ensemble-mean heights, and the (b) 72-h, (c) 96-h, and (d) 120-h ensemble-mean forecasts of SLP (black contours in hPa). Shading represents standard deviation (hPa) about the ensemble.	41
Figure 29.	The 0000 UTC 13 February analyzed SLP ensemble-mean heights, and the (b) 72-h, (c) 96-h, and (d) 120-h ensemble-mean forecasts of SLP (black contours in hPa). Shading represents standard deviation (hPa) about the ensemble.	42
Figure 30.	The 996 hPa contour for the ensemble members for the (a) analysis at 0000 UTC 7 February, the (b) 72-h forecast, and (c) 96-h forecast that verify at 0000 UTC 7 February. The black box defines the area of L1 over which the members are evaluated.	44
Figure 31.	The 996 hPa contour for the ensemble members for the (a) analysis at 0000 UTC 9 February and the (b) 72-h forecast that verifies at 0000 UTC 9 February. The black box defines the area of L2 over which the members are evaluated.....	45
Figure 32.	A comparison of the (a) 0000 UTC 10 February SLP analysis to the (b) 144-h forecast. The black box defines the area of L3 over which the members are evaluated.....	45
Figure 33.	The 540 dam contour for the ensemble members for the (a) analysis at 0000 UTC 11 February, the (b) 168-h forecast initialized 0000 UTC 4 February, and the (c) 144-h forecast initialized 5 February that verify at 0000 UTC 11 February.	46
Figure 34.	The 540 dam contour for the ensemble members for the (a) analysis at 0000 UTC 13 February and the (b) 192-h forecast initialized 0000 UTC 5 February that verify at 0000 UTC 13 February.	47

THIS PAGE INTENTIONALLY LEFT BLANK

LIST OF TABLES

Table 1.	A list of which ensemble members best forecast the synoptic features for forecasts initialized 3–10 February. Shading in a row defines a member providing the best forecast for a given feature.	49
----------	---	----

THIS PAGE INTENTIONALLY LEFT BLANK

LIST OF ACRONYMS AND ABBREVIATIONS

CCB	Cold Conveyor Belt
CFSR	Climate System Forecast Reanalysis
DAS	Dry Airstream
DoD	Department of Defense
DT	Dynamic Tropopause
EKE	Eddy Kinetic Energy
ESRL	Earth Science Research Laboratory
GEFS	Global Ensemble Forecast System
GFS	Global Forecast System
LC1	Life-Cycle 1
LC2	Life-Cycle 2
MSLP	Mean Surface Level Pressure
NATO	North Atlantic Treaty Organization
NESDIS	National Environmental, Satellite, Data, and Information System
NSA	Naval Support Activity
NOAA	National Oceanographic and Atmospheric Administration
PV	Potential Vorticity
PVU	Potential Vorticity Unit
SLP	Sea Level Pressure
WCB	Warm Conveyor Belt

THIS PAGE INTENTIONALLY LEFT BLANK

ACKNOWLEDGMENTS

Professor Patrick Harr

Professor Richard Moore

Dr. Heather Archambault

Mr. Robert Creasey

THIS PAGE INTENTIONALLY LEFT BLANK

I. INTRODUCTION

A. MOTIVATION

1. Cold Surge and Snowfall Event over Crete

On 13 February 2004, an extremely cold air mass from Romania, Bulgaria, and Ukraine, extended southward over the Aegean Sea reaching as far south as the northern coasts of Egypt and Libya. Similar synoptic environments over western Europe have been related to the formation of extratropical cyclones known as Genoa Lows, which occasionally result in significant flooding over regions surrounding the Mediterranean Sea (Trigo, Bigg, & Davies 2002). The cold air mass and associated cyclogenesis event examined in this study resulted in over 45 cm of snowfall in Souda Bay, Crete (Figure 1). Typically, a synoptic-scale event of such a large deviation from normal conditions is associated with several precursor events that lead to an extreme development. These events are often difficult to forecast as was the case for this particular event. Naval Support Activity (NSA) Souda Bay effectively ceased operations due to the snowfall. As the base did not have dedicated snow clearing equipment, Navy personnel were forced to clear the airfield and roads with shovels and bulldozers. The goal of this case study is to examine the dynamical processes that led to the extreme weather event and identify factors that could aid in forecasting similar events in the future.



Figure 1. Navy personnel clearing snow from a gate at Naval Support Activity Souda Bay and airfield, 13 February 2004 (From U.S. Navy archives).

The low pressure system that caused the snowfall event in Crete was related to a pre-existing low-level baroclinic zone over the Ionian Sea that connected to a Bora wind event in the Adriatic Sea on 12 February 2004. At upper levels, a highly amplified long-wave trough existed over eastern Europe. It is possible that the low-level baroclinicity further enhanced the long-wave trough as in a Petterson-Smebye (1971) type B scenario.

Although the case examined in this thesis was extreme, synoptic patterns that induce these outbreaks of cold air are common in the western and central Mediterranean. The Genoa Lows that form downstream of these cold surges cause significant wind and rain events and occasional flooding. As Department of Defense (DoD) and North Atlantic Treaty Organization (NATO) have several installations in areas affected by these storms, it is critical that forecasters understand and recognize scenarios favorable for development of storms to increase readiness and decrease response times for any associated hazardous weather.

2. Timeline

The sequence of events (Figure 2) that led to the cold surge over eastern Europe began nearly 10 days prior to the snow event on Crete. The first of three successive cyclones (L1) in the Atlantic formed on 6 February over the Labrador Sea. This system remained in the southern Labrador Sea for approximately 24 hours before moving north and filling the morning of 8 February. The second cyclone (L2) moved off the northeast coast of the United States the morning of 7 February. It rapidly deepened as it moved northeastward towards Greenland, eventually filling over southern Greenland on 9 February. The third cyclone formed in the central Atlantic on the trailing edge of the second cyclone early on 9 February. The third cyclone (L3) quickly moved northward until it started to fill at 1800 UTC 10 February. Downstream of the three cyclones a ridge amplified poleward. The maximum amplitude of this ridge also occurred at approximately 1800 UTC 10 February. The extreme amplitude of the ridge resulted in significant

downstream cold-air advection into central and eastern Europe, thereby contributing to the outbreak of anomalously cold air that affected Crete on 13 February (Figure 2).

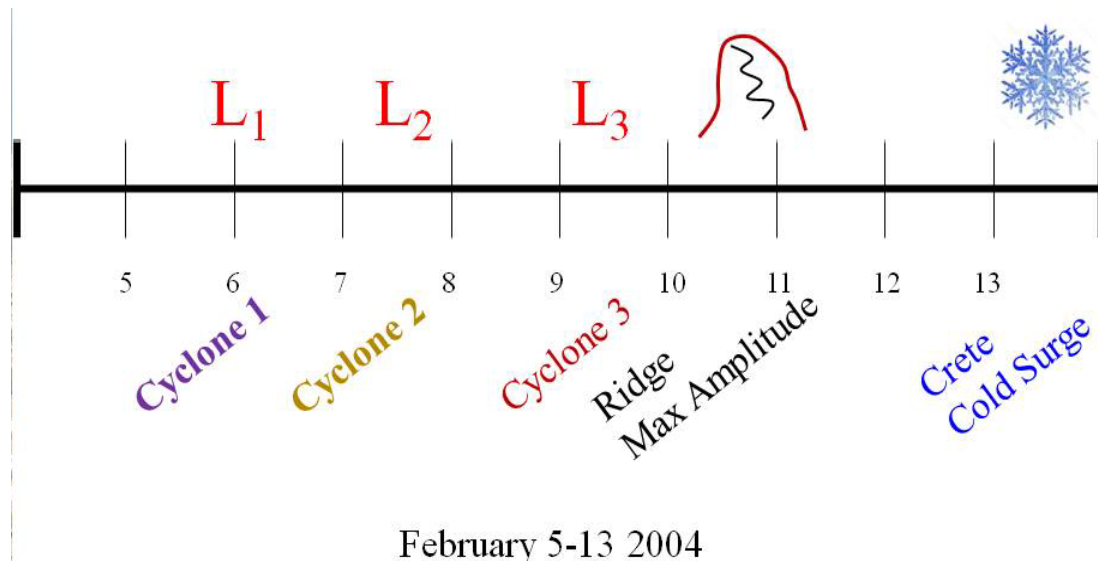


Figure 2. Timeline of synoptic weather events between 5–13 February 2004.

3. Ingredients for Development of the Extreme Cold Surge

As defined in Figure 2, several precursor events combined to contribute to the extreme cold surge. In particular, the sequence of cyclone events over the western Atlantic is examined with respect to forcing a high-amplitude ridge-trough system that developed over the north Atlantic and northern Europe.

a. Cyclone Development

An important aspect of the cyclone development is that each successive cyclone that formed between 6–10 February followed a more meridional-oriented track over the western north Atlantic. The southwesterly flow around the eastern flanks of the cyclones advected warm, moist air from the sub-tropical Atlantic to higher latitudes. The warm-air advection and related diabatic process from the three cyclones contributed to an extreme amplification of the sub-tropical Atlantic anticyclone.

b. Ridge Amplification

The building anticyclone defined a pattern similar to that of an atmospheric block over the northeast Atlantic and northwest Europe. However, the amplified ridge did not persist long enough, nor was the ridge stationary for classification as a blocking pattern (Altenhoff, Martius, Croci-Maspoli, Schwierz, & Davies 2008). As the ridge moved eastward, the northern extent amplified and resulted in significant cold-air advection along the eastern flank of the ridge over central Europe. Cold temperatures typically occur on the eastern flanks of large blocking patterns (Pfahl & Wernli 2012), and much of central and eastern Europe experienced anomalously low temperatures while under the influence of the northerly flow. The trough downstream of the northerly flow began to extend meridionally and thinned zonally, while also being oriented northeast to southwest. This is consistent with anticyclonic wave breaking.

4. Predictability

The weather over Crete on 13 February 2004 was highly anomalous due to both the total snowfall amount and the extreme cold. The high amplitude pattern and extreme conditions were not well forecast. The NSA Souda Bay Command Duty Officer log from 13 February 2004 has record of thunderstorm conditions and a freeze advisory, but nothing regarding snowfall. Because there were several synoptic-scale factors that led to the extreme cold outbreak, the source of forecast difficulty could be quite varied. Determination of the causes of synoptic factors that led to the ridge building, wave break, and cold surge will help forecasters identify features that might lead to similar events in the future. To evaluate the predictability of the high-impact event, ensemble reforecast data from the Global Forecast System (GFS) model and Climate Forecast System Reanalysis (CFSR) are used to examine model performance of the scenario, uncertainty in the forecasts, and the processes that led to the uncertainty.

B. OBJECTIVE

It is hypothesized that the primary predictability issue associated with the extreme cold surge over eastern Europe case was due to the development of the upstream ridge in the northern Atlantic. Furthermore, the ridge-building event was directly related to the development of cyclonic disturbances over the western North Atlantic and eastern North America.

This hypothesis is examined by examining the evolution of the building ridge in the Atlantic, and the impact of the deepening trough over central and eastern Europe. The cyclone development is examined in the context of the paradigm of baroclinic wave life cycles (Thorncroft, Hoskins, & McIntyre 1993) associated with cyclonic and anticyclonic wave breaking. The role of cyclone development upstream of the building ridge is examined as one of the elements required to build the ridge and the eventual deepening of the trough and snowfall event.

In this case, predictability is depicted by the spread in 10 ensemble members and one control member. The spread is examined with regard to the three cyclones in the northern Atlantic, the building ridge, and subsequent trough over Europe.

THIS PAGE INTENTIONALLY LEFT BLANK

II. BACKGROUND

In this thesis, the combination of successive cyclonic events and downstream ridge amplification are examined with respect to general synoptic-scale characteristics of large-scale flow patterns. The component of cyclone development that is relevant to downstream ridge building is the warm conveyor belt (WCB). The primary large-scale flow patterns associated with this case are examined with respect to typical baroclinic life cycles.

A. BAROCLINIC LIFE CYCLE CHARACTERISTICS

Thorncroft et al. (1993) investigated two characteristic baroclinic life cycles. In general, the life-cycle (LC) paradigm of Thorncroft, Hoskins, and McIntyre (1993) is a higher resolution version of the Simmons-Hoskins (1980) "basic" and "anomalous" cases, that depicts the decaying stages of eddy kinetic energy (EKE) as part of the baroclinic life cycle. The EKE is defined as the kinetic energy associated with turbulent flow. A baroclinic wave "breaks" when the material contours defining the wave are irreversibly deformed (McIntyre and Palmer, 1983). In the case of LC1, there is a rapid decay of EKE after reaching an EKE maximum (Figure 3). In the case of LC2, there is a slow decay of EKE. The two evolutions of EKE decay are evident at upper levels based on analysis of potential temperature on the nominal tropopause, which was defined as a constant potential vorticity (PVU) surface. Thorncroft et al. (1993) used the two potential vorticity unit (PVU, $1 \text{ PVU} = 10^{-6} \text{ K m}^2 \text{ kg}^{-1} \text{ s}^{-1}$) surface in their analysis. Due to the advective properties of PV and potential temperature, the PV-potential temperature field is useful in describing atmospheric characteristics that provide dynamical insight into complicated non-linear processes.

The initial perturbation for the Simmons-Hoskins cases refers to a mean zonal flow and a one hPa surface-pressure perturbation on day 0 (Thorncroft et al, 1993). An LC1 wave break (Figure 4b), also referred to as an anticyclonic wave break, is characterized when the ensuing midlatitude trough (Figure 4a)

thins with the mean anticyclonic horizontal shear that is present in the westerly flow. A thinning trough has a positive tilt downstream as it extends toward the subtropics to develop a northeast-southwest orientation. The zonal extent of the trough extent is reduced (i.e., thinned), and the meridional extent increases. The thinned trough is then advected anticyclonically and equatorward (Thorncroft et al., 1993). Baroclinic instability accounts for most of the wave and EKE growth through day 4 or 5 (Figure 2). The EKE in an LC1 wave typically reaches a maximum value on day 7, and the EKE maximum is predominantly on the southern, anticyclonic flank of the jet. After day 7, an LC1 wave decays in association with strong barotropic momentum fluxes from the trough into the jet that accompany a reduction in EKE by day 10 (Figure 3).

An LC2 wave (Figure 4c), also referred to as cyclonic wave breaking, is characterized by a wave that tilts against the mean flow and broadens with the cyclonic horizontal shear of the mean flow. An LC2 event develops a northwest to southeast orientation. The subtropical extension of the wave wraps cyclonically to often produce a major cut-off cyclone that moves poleward. The EKE maximum for an LC2 often occurs on the northern, cyclonic, flank of the mean flow, and it reaches a maximum on day 9 (Figure 3). The gradual decrease in EKE associated with an LC2 event suggests barotropic influences that act to decay the wave affects a LC2 wave less than LC1 waves.

The baroclinic life cycle paradigm as defined above is used to place the cold surge over eastern Europe into context of the overall synoptic-scale evolution. The life cycle paradigm will also be used to examine the predictability defined by individual ensemble member depictions of the wavebreaking event.

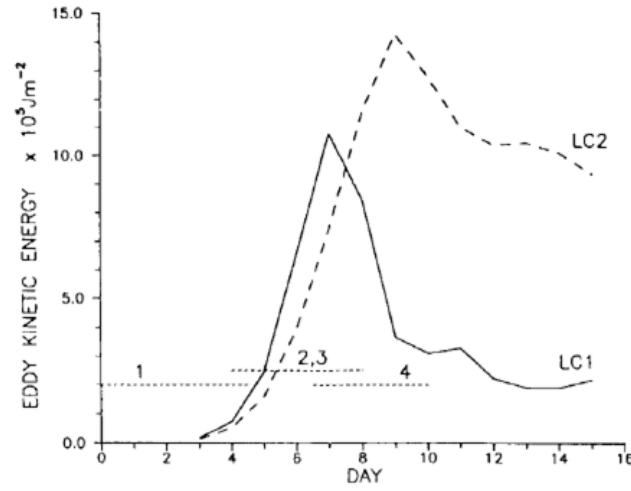


Figure 3. Eddy kinetic energy evolution for LC1 (dashed) and LC2 (solid). Day 0 is defined as the introduction of the small pressure perturbation into the mean zonal flow (From Thorncroft *et al.*, 1993).

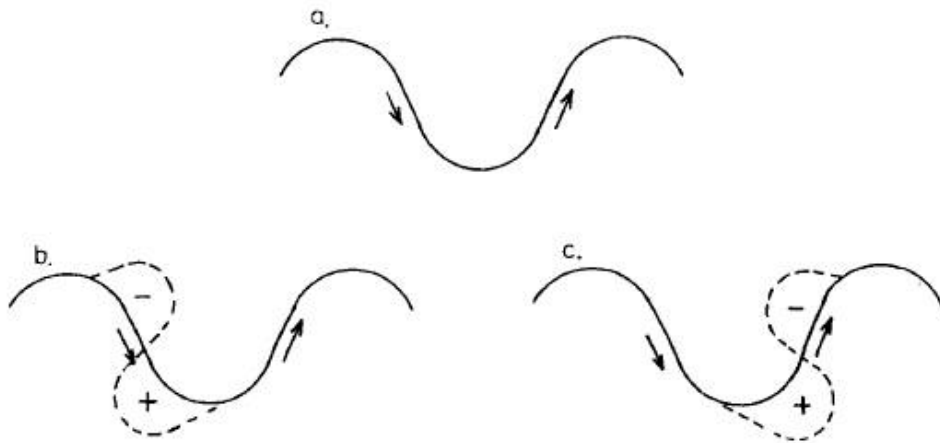


Figure 4. Schematic depicting (a) an initial perturbation before meridional wind shear has tilted the flow. The dashed line represents the flow after deformation from (b) anticyclonic tilting associated with an LC1 and (c) cyclonic tilting associated with an LC2 (From Thorncroft *et al.*, 1993).

B. WARM CONVEYOR BELT AND RIDGE BUILDING

Using a Lagrangian analysis, Carlson (1980) identified the structure of a mature cyclone as consisting of three primary airstreams (Figure 5); the warm conveyor belt (WCB), the cold conveyor belt (CCB), and the dry airstream (DAS). Carlson identified the coherent air streams, as having similar dynamic and thermodynamic evolutions. Each airstream contributed to the overall structure and characteristic comma-cloud pattern of a mature cyclone. In this analysis the primary focus is on the WCB as a key factor in ridge building.

Warm conveyor belts originate in the boundary layer of the equatorward portion of the cyclone warm sector. The WCB ascends ahead of the surface cold front (Joos & Wernli, 2012). The ascending air stream transports water vapor and heat poleward and to higher levels in the atmosphere. The WCB is responsible for most of the cyclone-related meridional energy transport. Furthermore, strong latent-heat release associated with clouds in the ascending portion of the WCB contributes to the meridional transport of heat in the mature cyclone.



Figure 5. Schematic of atmospheric conveyor belts. The WCB is depicted in orange (From University Corporation for Atmospheric Research).

To define WCB characteristics, Eckhardt, Stohl, Wernli, James, Forster, & Spichtinger (2004) defined several characteristic criteria. Approximately 60 percent of all WCBs are associated with extratropical cyclones (Eckhardt, Stohl, Wernli, James, Forster, & Spichtinger 2004), and WCBs are especially prominent in winter months. There are two predominant WCB starting regions in the Northern Hemisphere, east of North America and east of Asia, which correspond to the primary storm tracks of the western oceans (Figure 6). The WCB outflow regions in the upper troposphere are then located downstream off the west coasts of North America and Europe (Eckhardt et al., 2004).

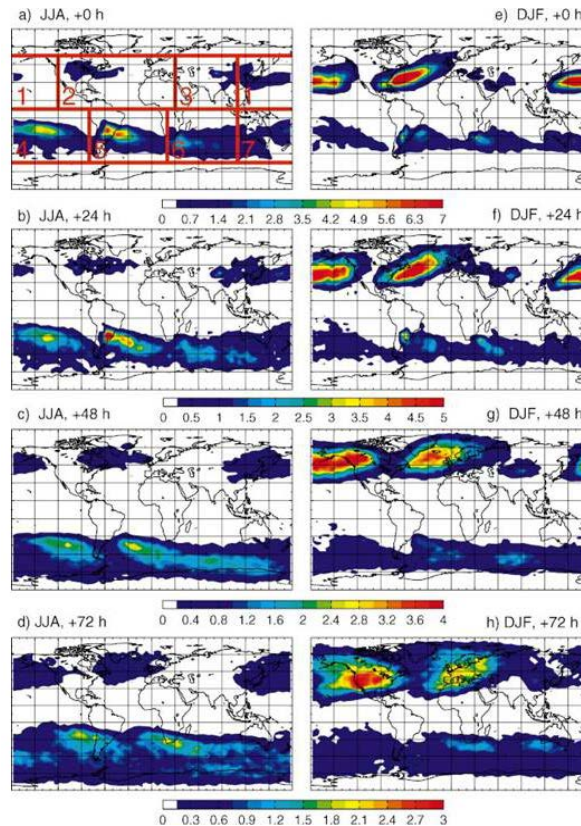


Figure 6. Seasonal mean spatial distribution of (a), WCB starting points and (e) WCB trajectory positions after (b) and (f) 24-h, (c) and (g) 48-h, (d) and (h) 72-h for (a)–(d) June–July–August and (e)–(g) December–January–February. Depicted is the fraction (in percent) of all trajectories that fulfill the WCB criteria, averaged over 15 years. Different color scales were used for different days for clarity. The red boxes in (a) used for additional analysis not shown here (From Eckhardt et al., 2004).

Under the influence of diabatic processes, PV is no longer conserved. The time tendency in PV is dependent on the vertical gradient in diabatic heating. Below the region of maximum heating, the PV tendency is positive (Figure 7). Above the region of maximum heating, the tendency of PV is negative (Figure 7). The upper-level negative PV anomaly results in upper-level ridging and may significantly modify the downstream flow (Figure 7). Therefore LC1 wavebreaking events frequently occur to the southeast of an enhanced ridge (Altenhoff et al., 2008). This is the scenario that will be investigated with respect to the cold surge event over eastern Europe in February 2004.

Due to the redistribution of PV associated with latent heat release, WCBs may affect the upper-tropospheric PV pattern (Pomeroy & Thorpe, 2000). The low-level positive PV anomalies produced by latent-heat release from condensation contribute up to 40 percent of the cyclonic circulation in a mature storm (Davis & Emanuel, 1991). Latent-heat release at upper-levels also increases static stability, creating a positive vorticity anomaly. Stoelinga (1996) argued that latent-heat release and the associated low-level PV maximum was responsible for up to 70 percent of the surface intensity of an extratropical cyclone.

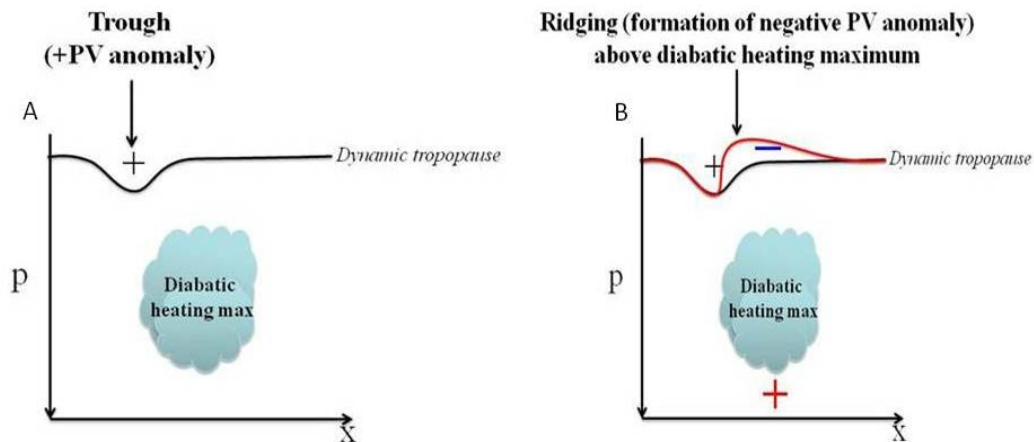


Figure 7. Depiction of the evolution of the dynamic tropopause (a) under the influence of an upper-level trough and positive potential vorticity anomaly and (b) subsequent downstream effects of mid-level diabatic heating on the PV tendency.

C. ENSEMBLE FORECASTING

Ensemble forecasting is a numerical prediction method that employs multiple model integrations each initiated with slightly different initial conditions (Kalnay 2006). It is assumed that the model is designed so that each forecast member is equally likely to occur. The differences in initial conditions are small and consistent with observation uncertainty. After several days, the initially small differences can yield substantially different forecasts. The variability among ensemble members is often taken as a measure of forecast uncertainty. By comparing different ensemble members, the forecast probability of a given weather event can be assessed (Kalnay 2006).

Ensemble forecasting can also be used to statistically post-process model-generated fields. Forecasters can identify errors with model output due to model bias, but systematic errors are more difficult to detect (Hamill & co-authors 2013). Using ensemble forecasting in case studies of past weather events, it may be possible to distinguish between random and model errors. Reforecasts have proven useful in model calibration for relatively rare, high-impact weather events (Hamill et al., 2008), and longer-lead weather-climate phenomena. Using associated observational data, estimates of a conditional distribution of possible outcomes are possible with current numerical guidance (Hamill et al., 2013).

THIS PAGE INTENTIONALLY LEFT BLANK

III. METHODOLOGY

A. DATA

All data were collected from various open sources and research communities. The time period of 1–17 February 2004 is analyzed for the North Atlantic Ocean, the Mediterranean Sea, and Europe.

1. Analysis Data

Analyzed data were obtained from the Global Forecast System (GFS) model utilizing Climate Forecast System Reanalysis (CFSR) (Saha and co-authors 2010). The global CFSR fields are produced at six-hour intervals and at a 0.5° latitude and longitude resolution and 64 vertical levels. To examine the climatological character of the extreme cold surge, temperature anomalies were retrieved using the Earth System Research Laboratory (ESRL) website (www.esrl.noaa.gov/psd/data/composites/day/). Temperature anomalies are defined relative to a 30 year (1981–2010) mean.

2. Satellite Imagery

Infrared and water vapor satellite imagery from GOES 12, Meteosat 5, and Meteosat 7, were collected from NOAA's National Environmental Satellite, Data, and Information (NESDID) archive. Satellite imagery was used to examine the evolution of the cyclonic systems, the WCB, and the downstream wavebreaking event.

B. PREDICTABILITY

The National Oceanographic and Atmospheric (NOAA) Global Ensemble Forecast System (GEFS) was used for this case study. The GEFS model forecasts are produced once daily for a 27-year period from 1985–2012. Each forecast consists of 10 ensemble members and all forecasts were constructed with the same model version, the same uncertainty parameterizations, and a similar method of ensemble initialization as currently used for the National

Centers for Environmental Prediction (NCEP) GEFS (Hamill et al., 2013). For the first week of time integration, each reforecast set is integrated at 0.5 degree grid spacing with 42 vertical levels. Beyond one week, forecasts were generated at 0.75 degree grid spacing and 42 vertical levels. Reforecasts were initialized using CFSR initial conditions. Perturbations were generated using the ensemble transform method and a rescaling technique (Hamill et al., 2013). The reforecasts were generated once per day at 0000 UTC.

C. DYNAMIC TROPOPAUSE

Potential vorticity is a conserved property in frictionless flow and under adiabatic conditions (Morgan & Nielsen-Gammon, 1997). Because of the conservation principle, PV is a useful parameter to characterize synoptic-scale flow. This enables characterizing synoptic-scale flows in terms of the PV distribution. Potential vorticity is particularly useful in diagnosing the characteristics of the tropopause as the gradient in static stability increases greatly at the tropopause (Hoskins et al., 1985). Due to high static stability, the stratosphere is a reservoir of high PV air. Because stretching and compression in the troposphere can lead to discontinuous changes in the location of a lapse-rate-defined tropopause, studies examining troposphere-stratosphere exchange frequently define the tropopause as a particular value of PV. A PV-defined tropopause, or “dynamic tropopause” (Danielsen & Hipskind, 1980), is more spatially continuous than a lapse-rate-defined tropopause.

Multiple values of PV have been used to define the tropopause. Typically, these values are between 1 and 3.5 PVU, as these tend to lie within the transition zone of the upper troposphere and lower stratosphere (Morgan & Nielsen-Gammon, 1997). In this thesis, the 2.0 PVU surface is used to define the dynamic tropopause.

Potential temperature is the temperature a parcel of air would have if adiabatically compressed or expanded from its original pressure to a reference pressure, usually 1000 hPa. Isentropic surfaces slope upward in cold air. The

opposing slopes of PV and potential temperature surfaces result in PV gradients along isentropic surfaces being sharper than along isobaric surfaces (Morgan & Nielsen-Gammon, 1997). Furthermore, the PV gradient is strongest near the tropopause due to rapid changes in static stability. Rossby waves in the upper troposphere interact with the instantaneous PV distribution, which makes it possible to analyze forcing of wave evolution and potential significant weather events by examining the instantaneous PV distribution (Morgan & Nielsen-Gammon, 1997).

D. STANDARDIZED ANOMALIES

To determine the magnitude of the anomalies in the North Atlantic ridge and central European trough discussed in this study, standardized anomaly plots were created. The anomalies in the 300 hPa, 500 hPa, and 925 hPa height fields were computed by subtracting the long-term, 21 day mean of 1979-2010 from the instantaneous value and then dividing by the long-term 21 day standard deviation (Hart & Grumm, 2001). The long-term mean and standard deviation values were obtained from the 2.5° latitude and longitude NCEP reanalysis. Anomaly plots were constructed at six-hour intervals from 0000 UTC 1 February through 1800 UTC 16 February.

Hart and Grumm (2001) defined an anomaly of four or more standard deviations as a rare event. Over the course of the annual cycle, a maximum of rare events exists during winter and a minimum in summer, but major departures from climatology are still possible in summer. Large departures are limited in summer because several nonlinear processes (frontogenesis, cyclogenesis, advection, and shear) that cause large anomalies are limited in summer. Large height anomalies are also maximized at lower latitudes (Hart & Grumm, 2001).

THIS PAGE INTENTIONALLY LEFT BLANK

IV. ANALYSIS AND RESULTS

A. PRECURSOR EVOLUTION: FEBRUARY 6-11 2004

The cold surge over the Aegean Sea and eastern Mediterranean can be traced back to an extreme amplification of a synoptic-scale transient ridge over the central Atlantic from 8–10 February 2004. Key factors to be discussed are the persistent warm-air advection over the central North Atlantic that contributed to the ridge building and extension, and anomalously cold air that moved into central and eastern Europe. The maximum cold-air advection occurred between 11–12 February on the eastern flank of the building ridge. Cold air moved over Scandinavia on 11 February then extended southward on 12 February (Figure 8). The anomalously cold air began flowing into the Aegean and eastern Mediterranean on 13 February. The maximum cold anomaly of -12°C occurred over the Aegean Sea on 13 February. Warm air moved eastward over high latitudes, replacing the cold anomalies over Scandinavia and western Europe on 13 and 14 February. The maximum warm anomaly occurs over northern Sweden and Finland on 13 and 14 February.

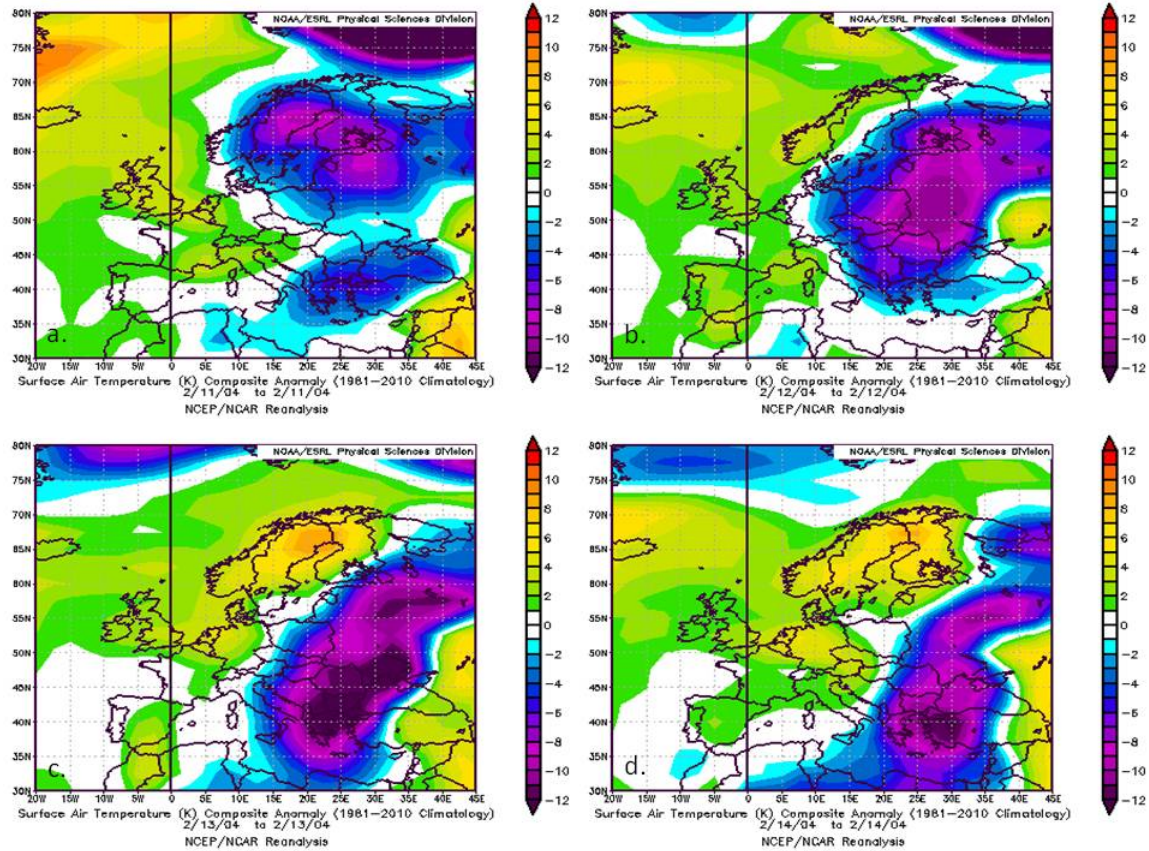


Figure 8. Surface temperature anomalies over 24 hours in degrees Kelvin over Europe for (a) 11 February, (b) 12 February, (c) 13 February, and (d) 14 February. Image created using the Earth System Research Laboratory Physical Sciences Division website (<http://www.esrl.noaa.gov/psd/data/composites/day/>).

The timeline of Figure 2 is augmented in Figure 9 to denote the ridge building events in the North Atlantic. The evolution of ridge amplification is discussed in relation to successive cyclone events as depicted by the distribution of winds and potential temperature on the dynamic tropopause (DT). The first cyclone (L1) that contributed to the ridge amplification entered the Labrador Sea on 6 February (Figure 10a) with a central sea-level pressure (SLP) minimum of 992 hPa (Figure 11). This system remained in the Labrador Sea until it weakened on 8 February (Figure 10c). The cyclone, L1, allowed for an initial advection of warm air northward. The southwesterly winds along the eastern flank of the low in the Labrador Sea advected warm air to higher latitudes, which

contributed to the first ridge as represented by the increase of potential temperature on the DT analyzed along 42°W (Figures 10a, 10b) and extended southeastward to 44°N 23°W.

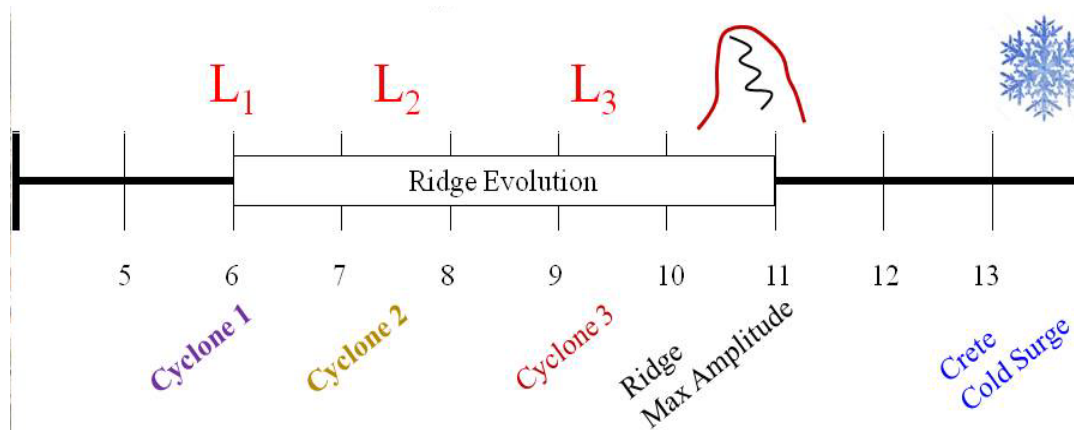


Figure 9. Timeline of synoptic weather events 5–13 February 2004 with emphasis on ridge amplification in the north Atlantic 6–10 February.

The trough associated with the cyclone in the Labrador Sea quickly thinned as a second cyclone (L2) formed off the New England coast on 7 February (Figure 10b) and rapidly deepened. The cyclone, L2, entered the western Atlantic with a SLP of 996 hPa at 1200 UTC 7 February (Figure 11). As L2 deepened and moved northeastward, the WCB associated with this cyclone contributed to the thinning of the trough that extended southward from L1 over the Labrador Sea. Between 0600 UTC and 1200 UTC 8 February, the minimum central pressure of L2 decreased from 976 hPa to 964 hPa (Figure 11). In association with the deepening of L2, the WCB increased and warm-air advection contributed to significant ridge building that extended to the northeast.

The distribution of potential temperature and winds on the DT accounts for the influence of warm-air advection on the building ridge. However, isolated regions of high potential temperature (i.e., elevated tropopause) are suggestive of diabatic contributions to the ridge-building event. While advective changes in the elevation of the DT dominate at 0000 UTC 8 February (Figure 10c), isolated regions of high potential temperature exist at 44°N 35°W on 0000 UTC 9

February (Figure 10d). This 24-h period encompassed the maximum deepening of L2 and increased WCB. The satellite image (Figure 12) confirms the presence of significant cloud cover that would be consistent with diabatic contributions to the elevated tropopause.

By 0000 UTC 10 February, a third cyclone (L3) (Figure 10e) formed in the central North Atlantic as a secondary cyclone on the trailing edge of L2. A closed circulation formed with a SLP of 992 hPa at approximately 0600 UTC 9 February near 42°N 35°W (Figure 12). The cyclone, L3, moved northward but did not significantly deepen until approximately 10 February, which was when L2 moved over Greenland and significantly weakened. The building ridge due to L2 forced L3 to move in a meridional direction (Figure 11). The position and track of L3 contributed to additional warm-air advection and amplification of the ridge over the central Atlantic. As defined in the sequence of DT charts (Figures 10a–10e), the primary North Atlantic ridge built with each successive cyclone; L1, L2, and L3. The evolution of the ridge amplification is depicted in Figure 13. The greatest amplification of the ridge on the DT occurred between 9 and 10 February under the influence of the WCB and meridional track of L3. The cyclone, L3 reached peak intensity of 972 hPa SLP at 1200 UTC 10 February, and the amplitude of the ridge reached its most northerly extent of 70.5°N at approximately 1800 UTC 10 February (Figure 13).

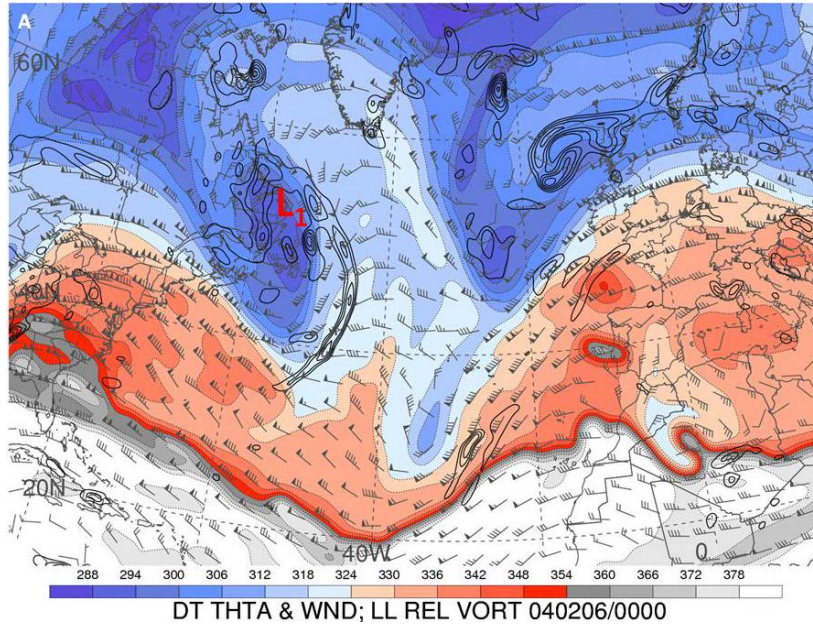


Figure 10. Potential temperature and winds on the dynamic tropopause (DT) at (a) 0000 UTC 6 February, (b) 0000 UTC 7 February, (c) 0000 8 February, (d) 0000 UTC 9 February, and (e) 0000 UTC 10 February. 10e also defines the WCB at 0000 UTC 10 February. The DT is defined as the 2.0 PVU surface. Potential temperature (K) on the DT is defined by the shading. Winds on the DT are defined by the barbs, and one large barb is defined as 5 m s^{-1} . Layer-averaged relative vorticity between 925 and 850 hPa is defined by the solid black contours. The L's define the circulation center of the three cyclones at the surface.

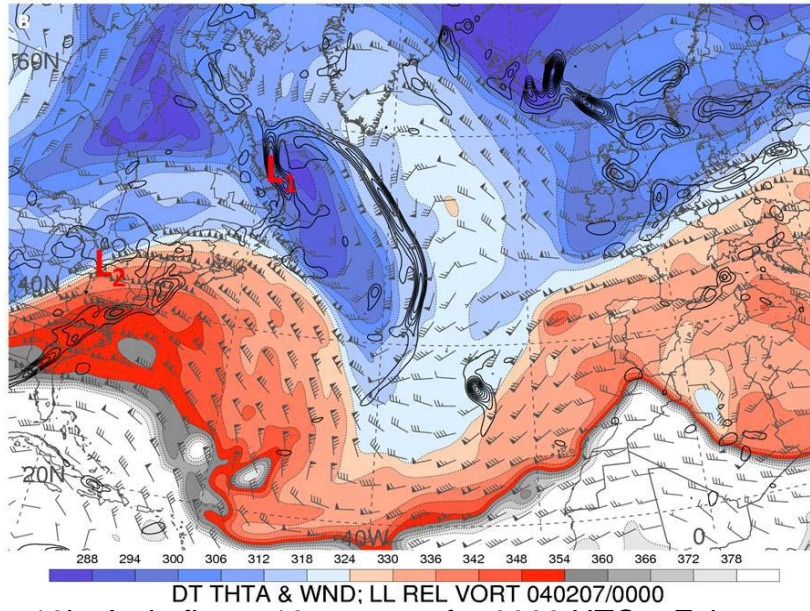


Figure 10b. As in figure 10a, except for 0000 UTC 7 February.

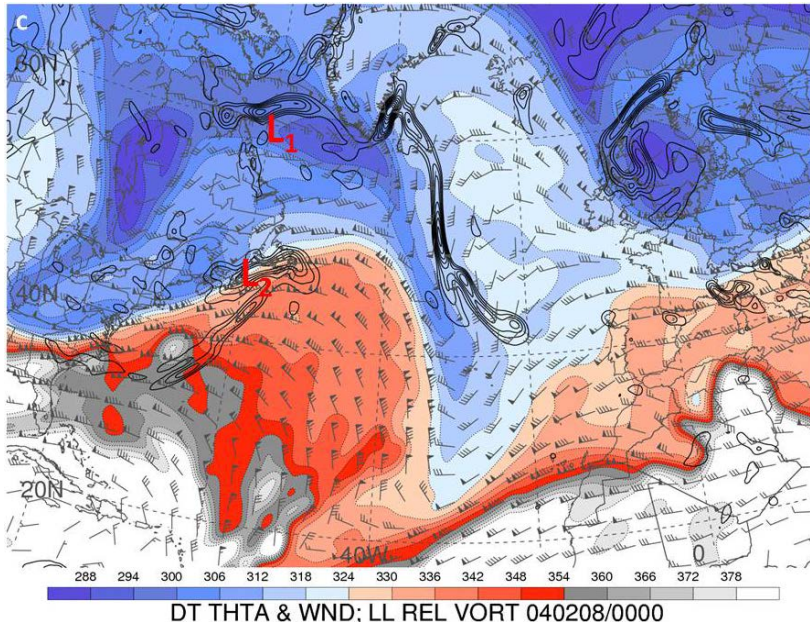


Figure 10c. As in figure 10a, except for 0000 UTC 8 February.

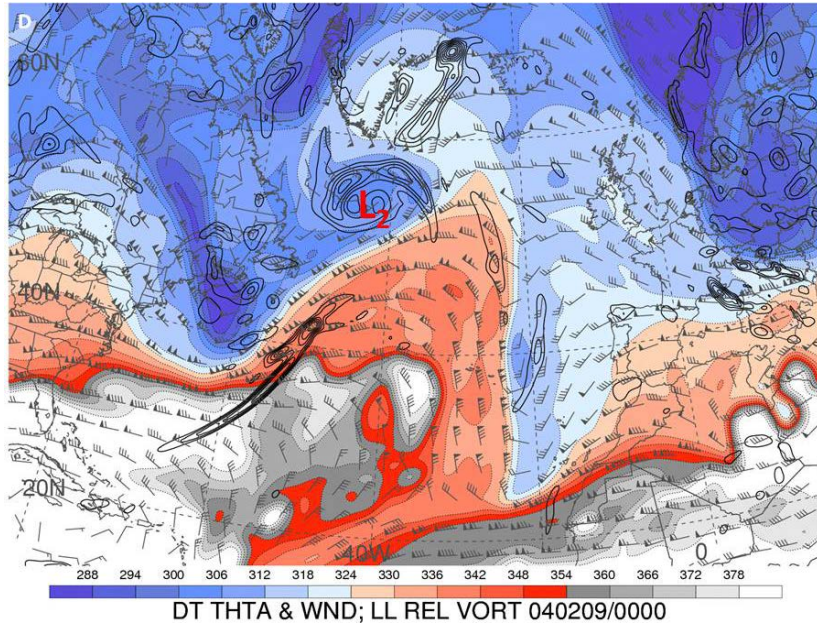


Figure 10d. As in figure 10a, except for 0000 UTC 9 February.

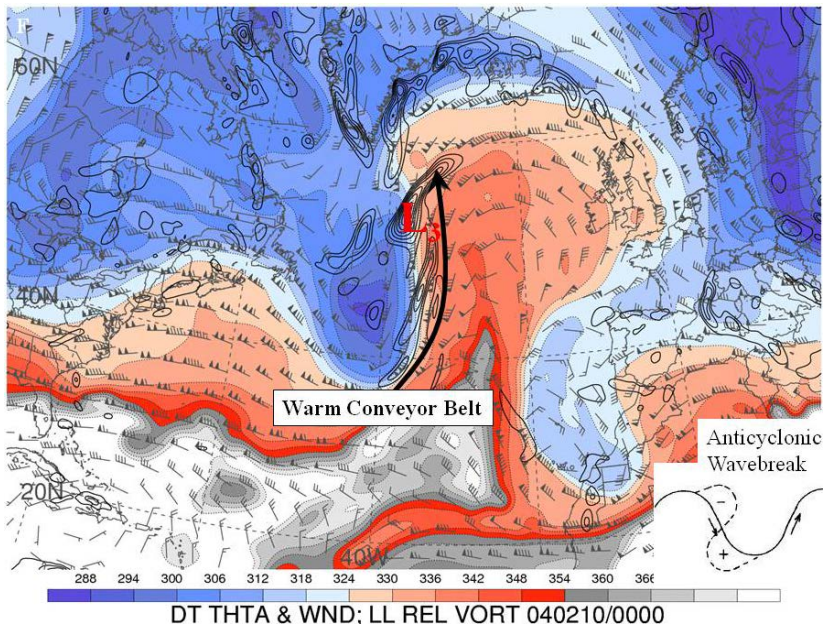


Figure 10e. As in figure 10a, except for 0000 UTC 10 February. Additionally, the black arrow defines the WCB associated with L3. The schematic is of an anticyclonic wavebreak as depicted in the inset.

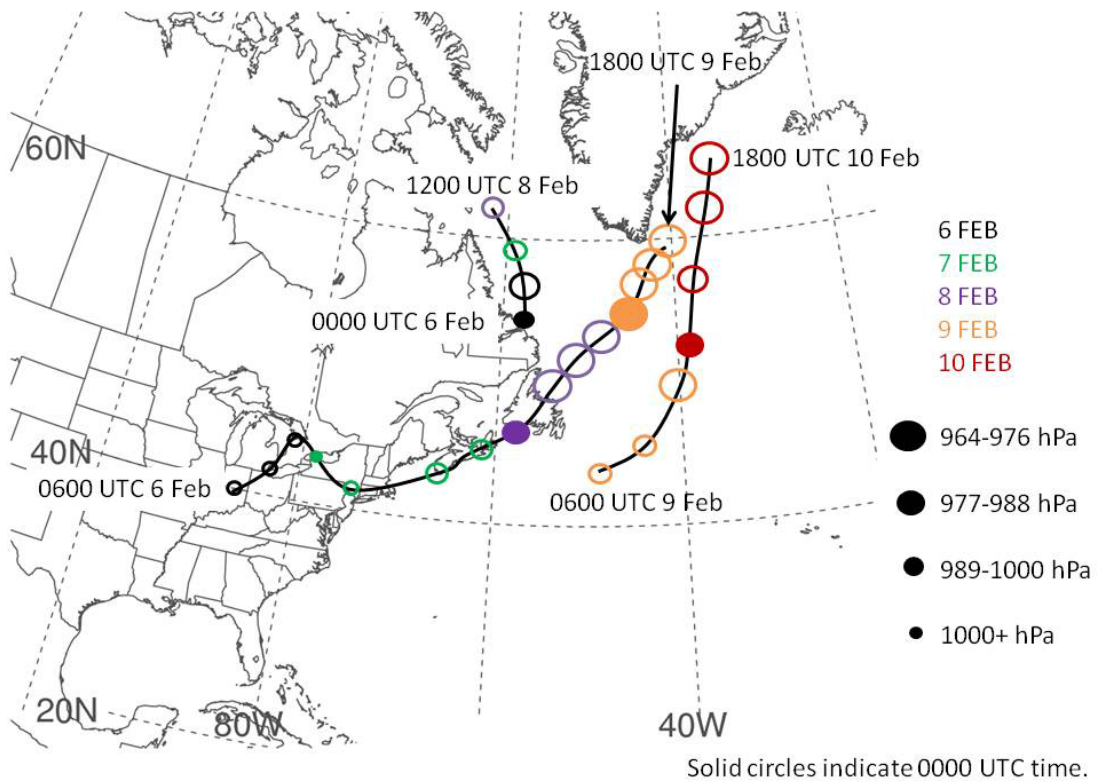


Figure 11. Tracks of three midlatitude cyclones defined in Figures 10a–10e. The circle size represents minimum sea-level pressure for the date time. Color coding defines the date.

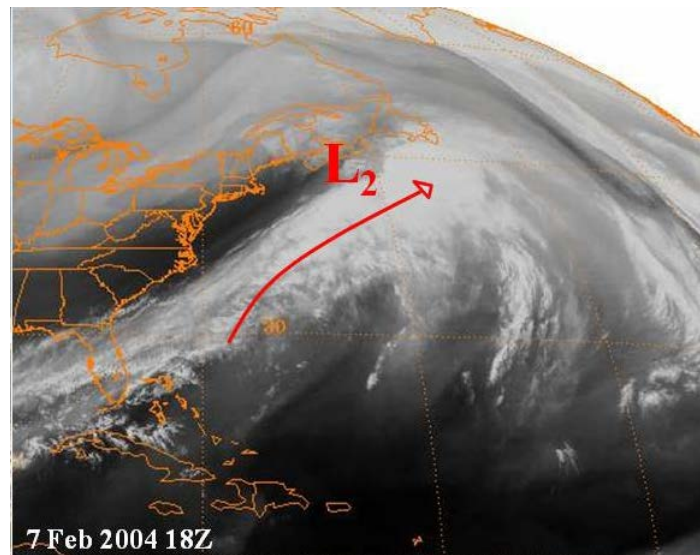


Figure 12. Water vapor satellite image from GOES 12 for 1800 UTC 7 February. The red line defines the WCB associated with L2.

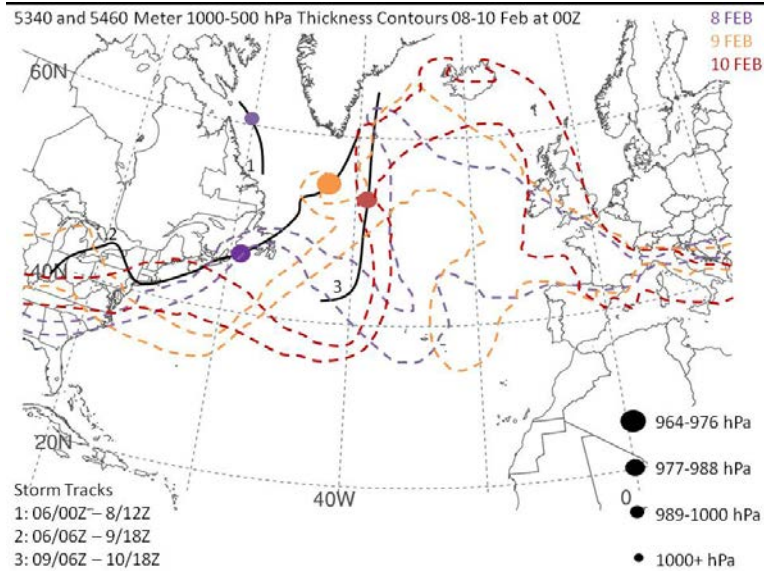


Figure 13. Depiction of ridge amplification over central North Atlantic as defined by the 5340 m and 5460 m 1000–500 hPa thickness. Tracks of cyclones identified in Figures 10a–10e are defined by the solid black lines. Color coding defines the dates.

To determine the significance of the Atlantic ridge at 1800 UTC 10 February, standard anomaly plots of geopotential heights at 925 hPa, 500 hPa, and 300 hPa were constructed. The standardization of the height anomalies and assumption of a normal distribution allows the anomalies to be defined as standard deviations from the mean, which is a measure of statistical significance with respect to climatology (Hart & Grumm 2001).

At the time of the maximum ridge amplitude, the anomaly in the Atlantic ridge at 300 hPa was two standard deviations above the mean, this value was only observed over a small region southeast of Iceland (Figure 14). Based on the assumption of a normal distribution associated with the standardized anomalies, (Hart & Grumm 2001), phenomena that are two standard deviations greater than the mean account for 2.5% of such events. The 500 hPa anomaly was less than two standard deviations (Figure 15), and the 925 anomaly was less than one standard deviation (Figure 16). The relatively low significance is likely due to the extreme variability of heights at such high latitudes.

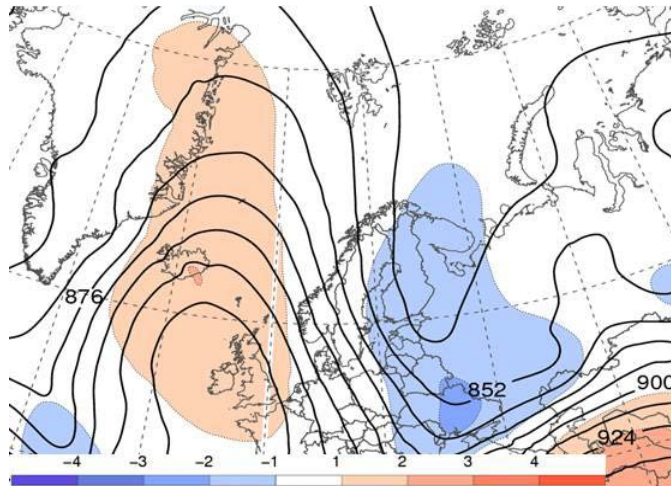


Figure 14. The 1800 UTC 10 February 300 hPa heights (dam, black lines) and standardized anomalies (shading) defined as standard.

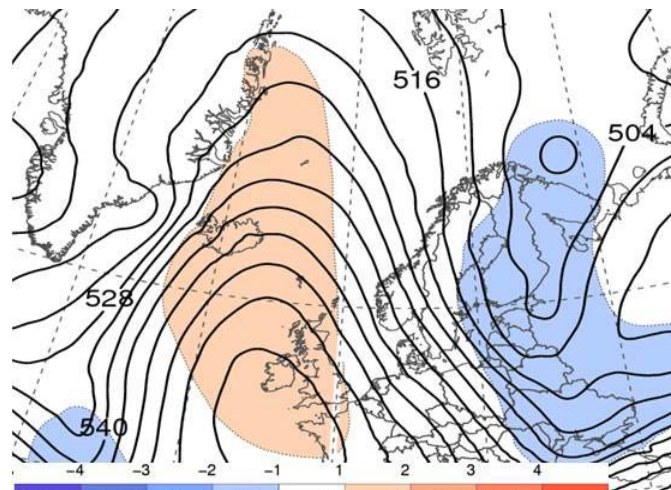


Figure 15. The 1800 UTC 10 February 500 hPa heights (dam, black lines) and standardized anomalies (shading) defined as standard deviations.

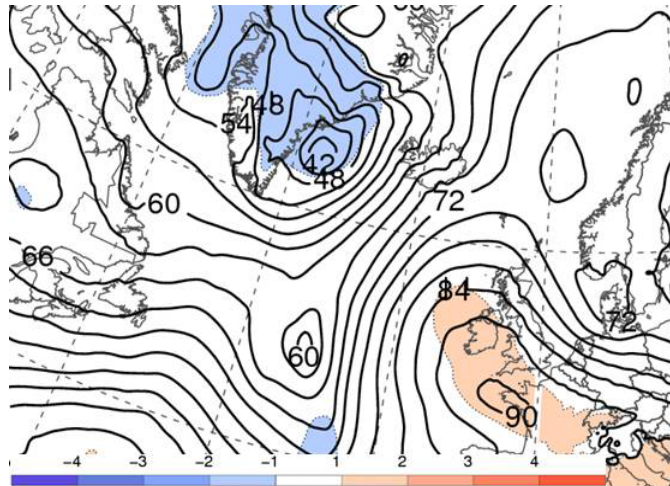


Figure 16. The 1800 UTC 10 February 925 hPa heights (dam, black lines) and standardized anomalies (shading) defined as standard deviations.

B. WAVEBREAK AND COLD SURGE

As depicted in the timeline (Figure 17), the anticyclonic wavebreaking and cold surge events occurred immediately following the ridge amplification over the north Atlantic. Therefore, the linkage between the two events is examined in the context of the LC1 wave lifecycle.

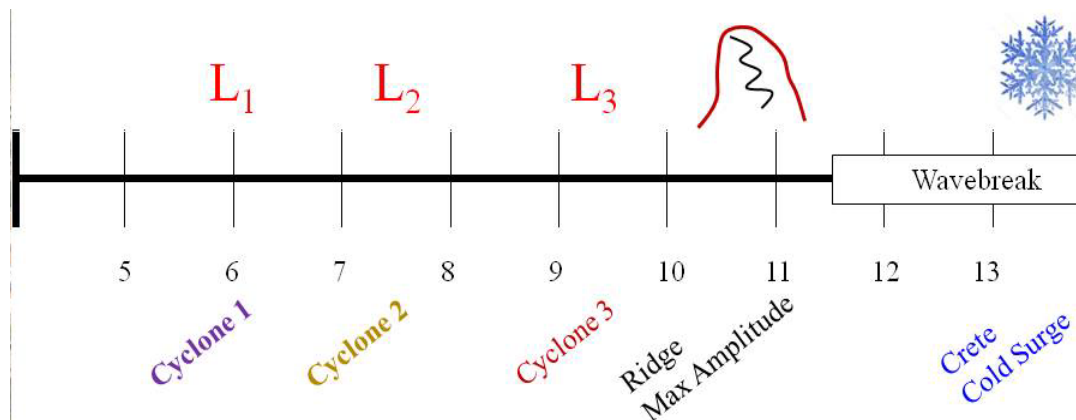


Figure 17. Timeline of synoptic weather events 5–13 February 2004 with emphasis on the anticyclonic wavebreak over Europe 11–12 February.

Between 11–13 February (Figures 18a–18c), the potential temperature gradient on the DT significantly increased on the eastern flank of the Atlantic

ridge. The steeply sloped DT was indicative of a strong northerly jet that extended from the northeast to the southwest into central Europe (Figure 18a). Also during this period, the ridge-trough couplet began to exhibit the characteristic northeast to southwest orientation associated with an anticyclonic wavebreak (Figures 18a). As the eastern flank of the ridge extended southeastward, the trough deepened. The characteristic “hook” of potential temperature on the DT (Figure 18a) became modified as the trough thinned over the next 24 h (Figure 18b). Eventually, a pocket of low potential temperature formed at the base of the trough over southeast Europe (Figure 18b). The extension and thinning of the trough resulted in the region of very low potential temperature separating from the main trough that was passing to the northeast (Figure 18c).

The trough in the DT and its associated positive PV anomaly spread over a low-level baroclinic zone that existed over central Europe on 11 February (Figure 18a, 18b). The vertical linkage between an upper-level positive PV anomaly and a low-level baroclinic zone are typical synoptic-scale factors that lead to Pettersen-Smebye type B cyclogenesis (Pettersen & Smebye 1971). The surface trough extended southwest from a low-pressure center in Russia and developed a closed cyclonic circulation at 1200 UTC 12 February (Figure 18b) over western Turkey that persisted for approximately 18 hours. It was during this period that a cold front passed over Crete in the early morning hours of 13 February. The trough in the DT reached its most southern extent at 1200 UTC 13 February (Figure 18c). Surface temperatures at this time were -1°C . Based on information from the Hellenic National Meteorological Service, this corresponds with surface temperatures in Crete that were 8°C to 9°C below the February average minimum temperature for Souda Bay (Figure 8).

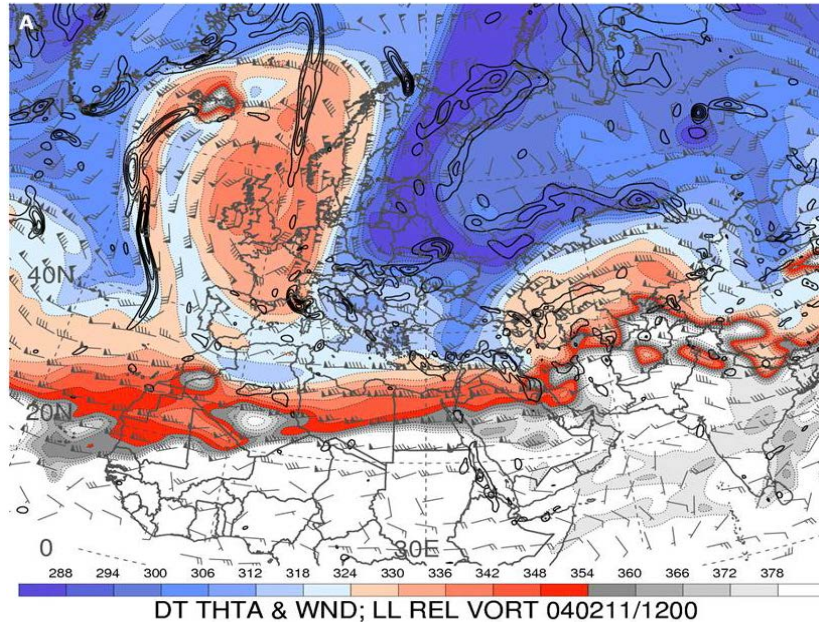


Figure 18. As in Figure 10a, except for (a) 1200 UTC 11 February, (b) 1200 UTC 12 February, and (c) 1200 UTC 13 February

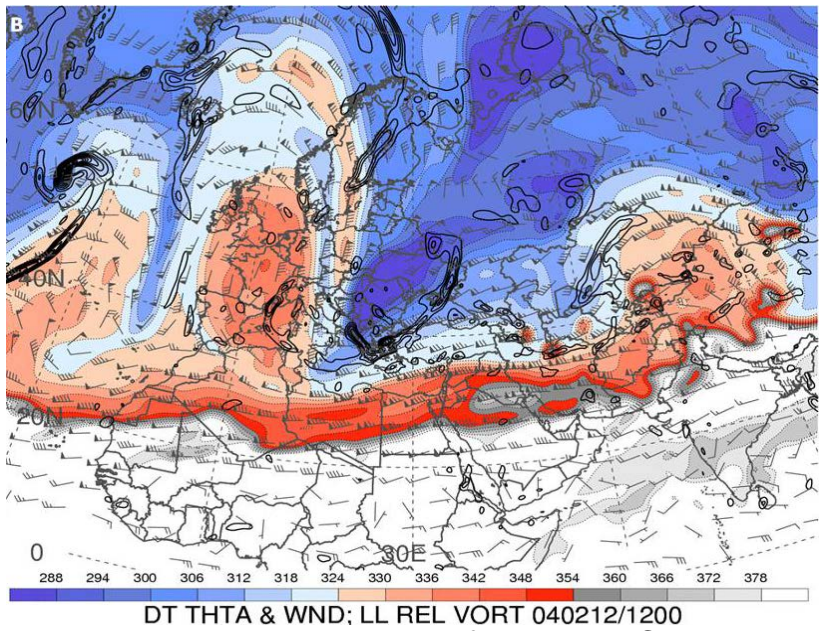


Figure 18b. As in Figure 10 a, except for 1200 UTC 12 February.

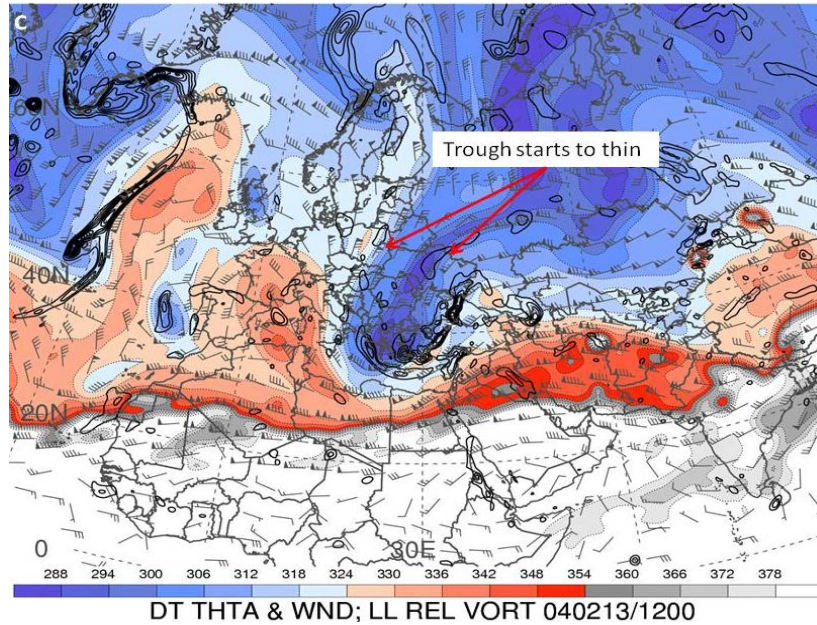


Figure 18c. As in Figure 10a, except for 1200 UTC 13 February.

The significance of the trough over eastern Europe is also analyzed using standardized height anomalies. Based on the standardized height anomalies (Figures 19–21), the trough over eastern Europe was more significant with respect to climatology than the ridge. The 300 hPa (Figure 19) and 500 hPa (Figure 20) geopotential height anomalies depict regions that are three standard deviations below the long term mean over the Aegean Sea. Anomalies of that magnitude occur one to two times per month (Hart & Grumm 2001). Despite the cold anomalies of 8–9°C below the February mean temperature at Chania and Souda Bay, the 925 hPa height anomaly was only one standard deviation below the long term mean (Figure 21). However, the large-scale trough was three standard deviations below the mean which is highly significant with respect to climatology.

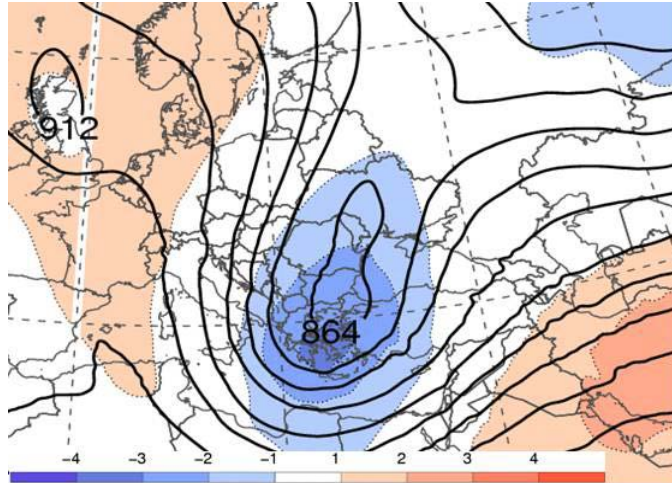


Figure 19. The 1200 UTC 13 February 300 hPa heights (dam, black lines) and standardized anomalies (shading) defined as standard deviations.

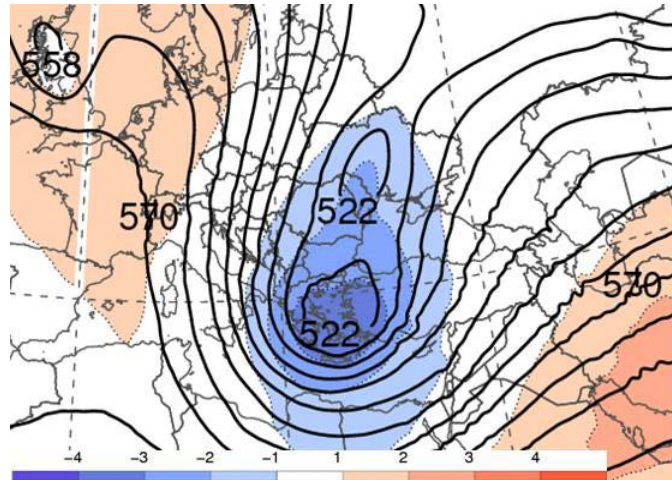


Figure 20. The 1200 UTC 13 February 500 hPa heights (dam, black lines) and standardized anomalies (shading) defined as standard deviations.

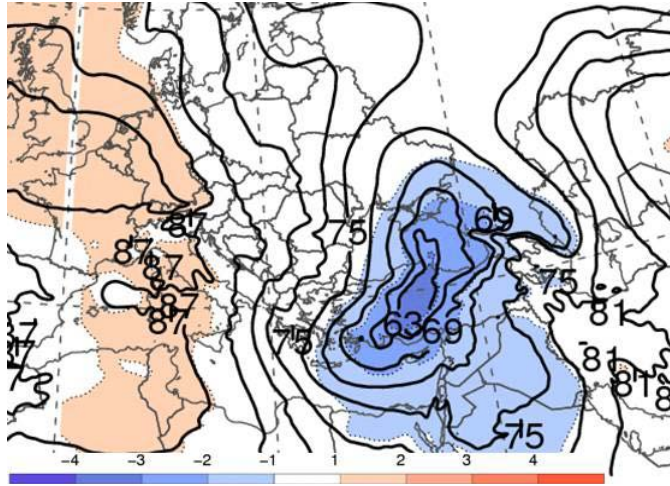


Figure 21. The 1200 UTC 13 February 925 hPa heights (dam, black lines) and standardized anomalies (shading) defined as standard deviations

Vertical cross sections (Figures 22 and 23) through the base of the deep trough that extended southward to Crete are used to depict the vertical distribution of PV, temperature advection, and the DT. At 0000 UTC 13 February (Figure 22), which is near the time of maximum trough amplitude, a narrow strip of high PV air descended to nearly 750 hPa over Crete. The backing winds to the west of the stratospheric intrusion define cold-air advection. Cold-air advection suggests the surface cyclone will deepen in the presence of extremely high PV air that is contained in the tropopause fold above Crete. Similarly, the veering winds to the east of the intrusion define warm-air advection and ascent. The warm-air advection to the east of the trough contributed to a steep gradient in the orientation of the tropopause.

The vertical cross section at 1200 UTC 13 February (Figure 23) indicates that the low-level cold air has moved eastward and deepened in the vertical. Significant cold-air advection exists to the level of 650 hPa. The fold in the tropopause that existed at 0000 UTC 13 February (Figure 22) has become a broad depression that is typical of a cold, upper-level cyclone.

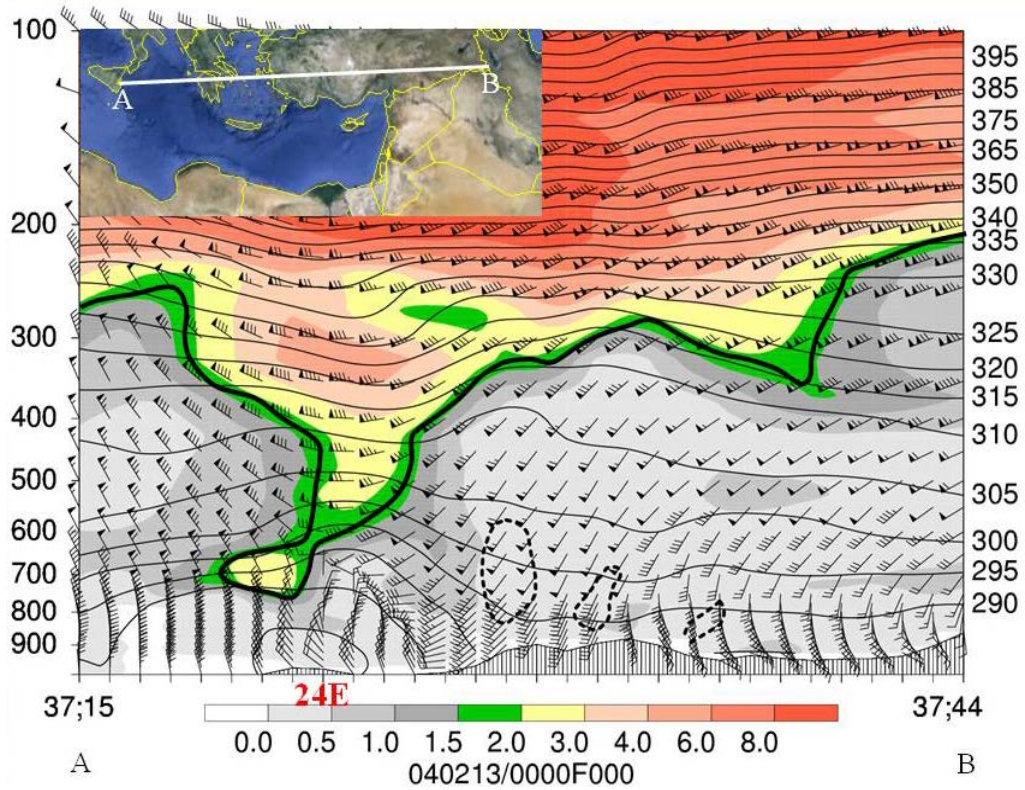


Figure 22. Vertical cross section for 0000 UTC 13 February with end points A and B defined by the inset map. The solid black line defines the tropopause, the long wind barbs define 5 m s^{-1} , flags define 25 m s^{-1} , shading defines potential vorticity in PVU, and the dashed black define ascent in $10^{-4} \text{ hPa s}^{-1}$. Souda Bay is located at 24°E longitude.

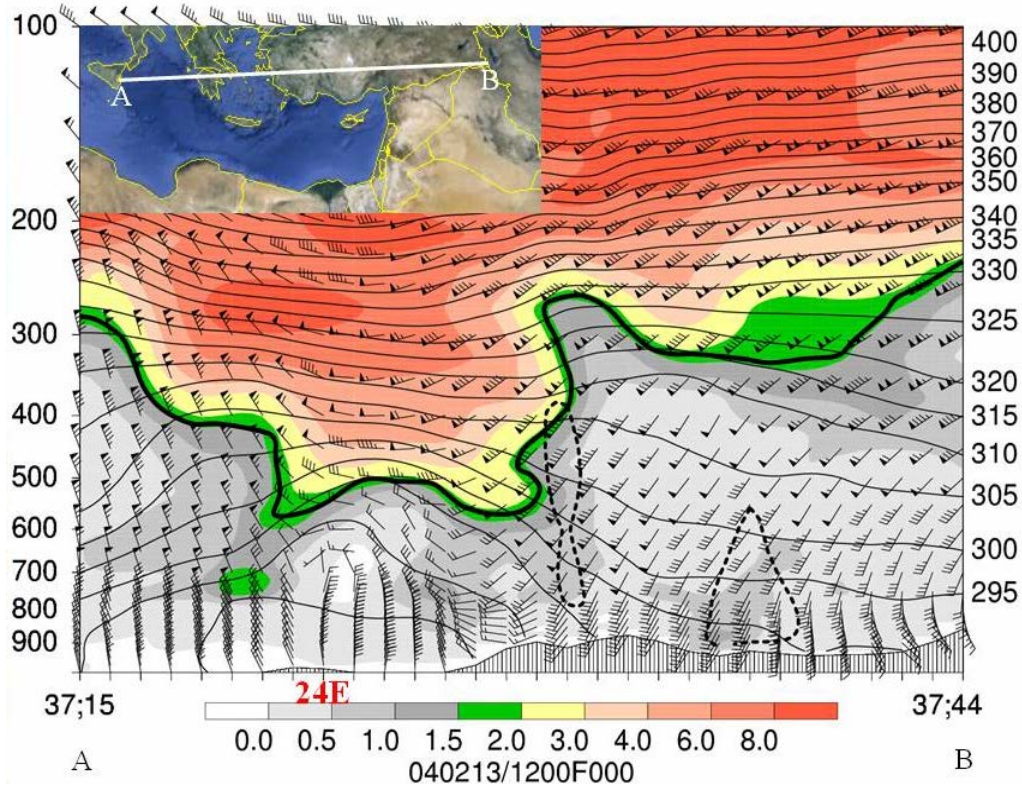


Figure 23. Vertical cross section for 1200 UTC 13 February with end points A and B defined by the inset map. The solid black line defines the tropopause, the wind barbs define 5 m s^{-1} , flags define 25 m s^{-1} , shading defines potential vorticity in PVU, and the dashed black define ascent in $10^{-4} \text{ hPa s}^{-1}$. Souda Bay is located at 24°E longitude.

C. PREDICTABILITY

The predictability of the cold surge will be examined using ensemble forecasts that verify during the period 11–13 February. This period encompasses the maximum amplitude of the ridge and the subsequent anticyclonic wavebreak. Examination of the spread among ensemble members begins at the 72-h forecast. For all forecasts verifying at 0000 UTC 11 February (Figure 24), the spread among ensemble members is concentrated over two regions of the ridge-trough system. At the apex of the ridge, spread increases over the northwest side between Iceland and Greenland. The magnitude of the spread increases as the forecast interval increases (Figures 24b–24d).

The second area of large spread is located on the eastern flank of the North Atlantic ridge and extends into the base of the deepening trough. While the magnitude of spread over the region increases with forecast range, it is not as large as the spread at the apex of the ridge.

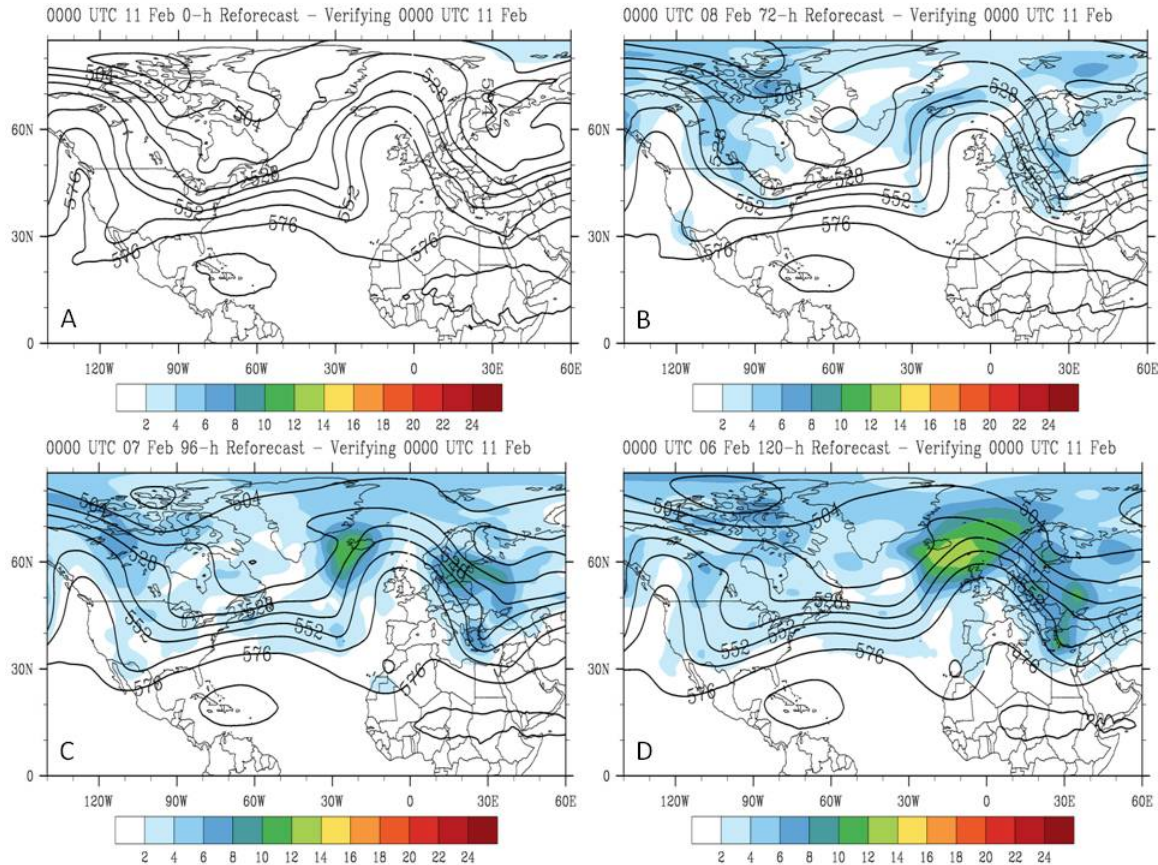


Figure 24. The 0000 UTC 11 February analyzed 500 hPa ensemble-mean heights, and the (b) 72-h, (c) 96-h, and (d) 120-h ensemble-mean forecasts of 500 hPa heights (black contours in dam). Shading represents standard deviation (m) about the ensemble.

Ensemble forecasts verifying at 12 February also contain significant uncertainty associated with the ridge-trough couplet (Figure 25) between Iceland and Greenland. While the ensemble spread increases with forecast interval, the magnitude of the spread in the trough is larger than the spread in the ridge. Therefore, uncertainty in forecasts has moved downstream over time.

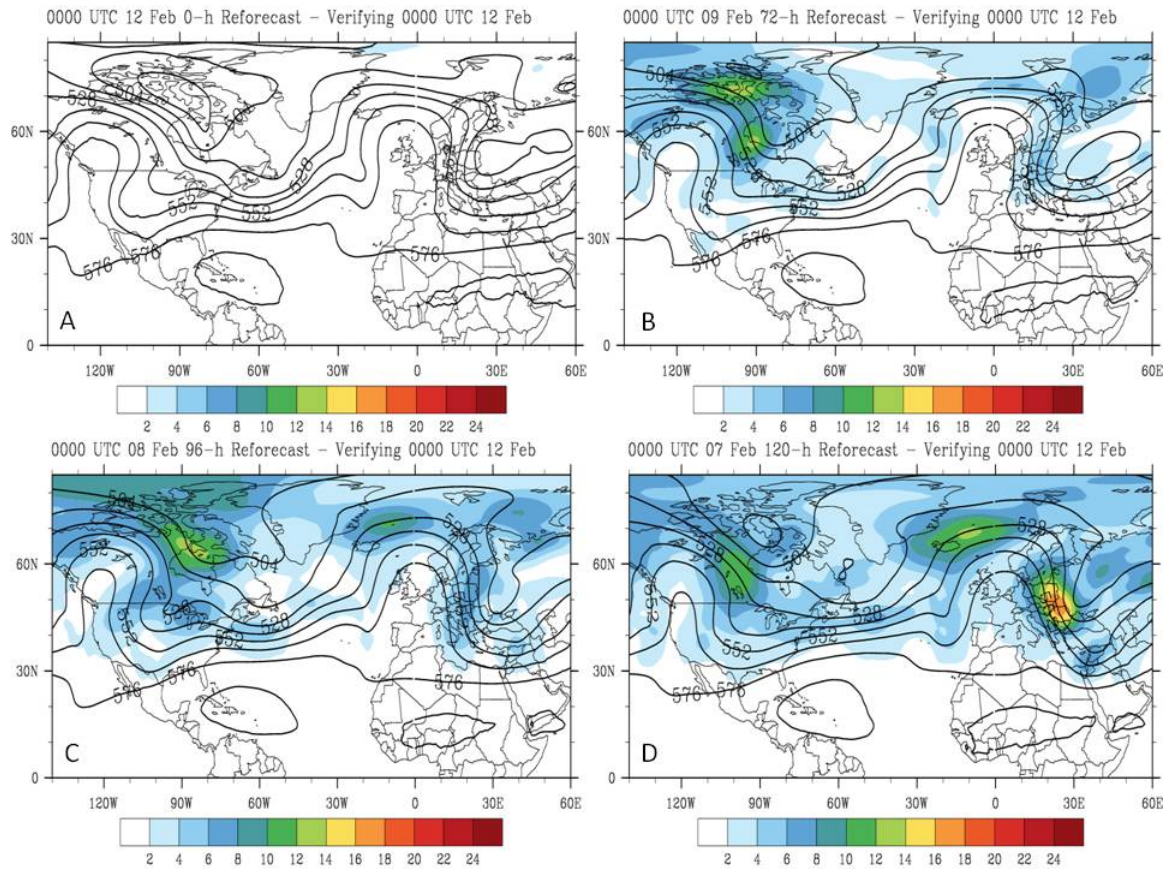


Figure 25. The 0000 UTC 12 February analyzed 500 hPa ensemble-mean heights, and the (b) 72-h, (c) 96-h, and (d) 120-h ensemble-mean forecasts of 500 hPa heights (black contours in dam). Shading represents standard deviation (m) about the ensemble.

Overall, uncertainty in forecasts verifying on 13 February (Figure 26) has decreased. In general, the uncertainty is concentrated over the eastern flank of the ridge that defines the cold-air advection into the base of the deepening trough. The 72-h (Figure 26b) and 96-h (Figure 26c) forecasts place the uncertainty west of the base of the trough, but the 120-h forecast (Figure 26d) places the uncertainty farther north. The 120-h forecast, initialized 8 February, also depicts less of an anticyclonic wavebreak orientation in the trough. Forecasts from the 8 February initialization were the first to exhibit significant uncertainty in forecasting the ridge on 11 February. The difficulty of the 8 February initialization in forecasting the subsequent ridge further supports the

hypothesis that accurate forecasting of the trough relies on an accurate forecast of the ridge.

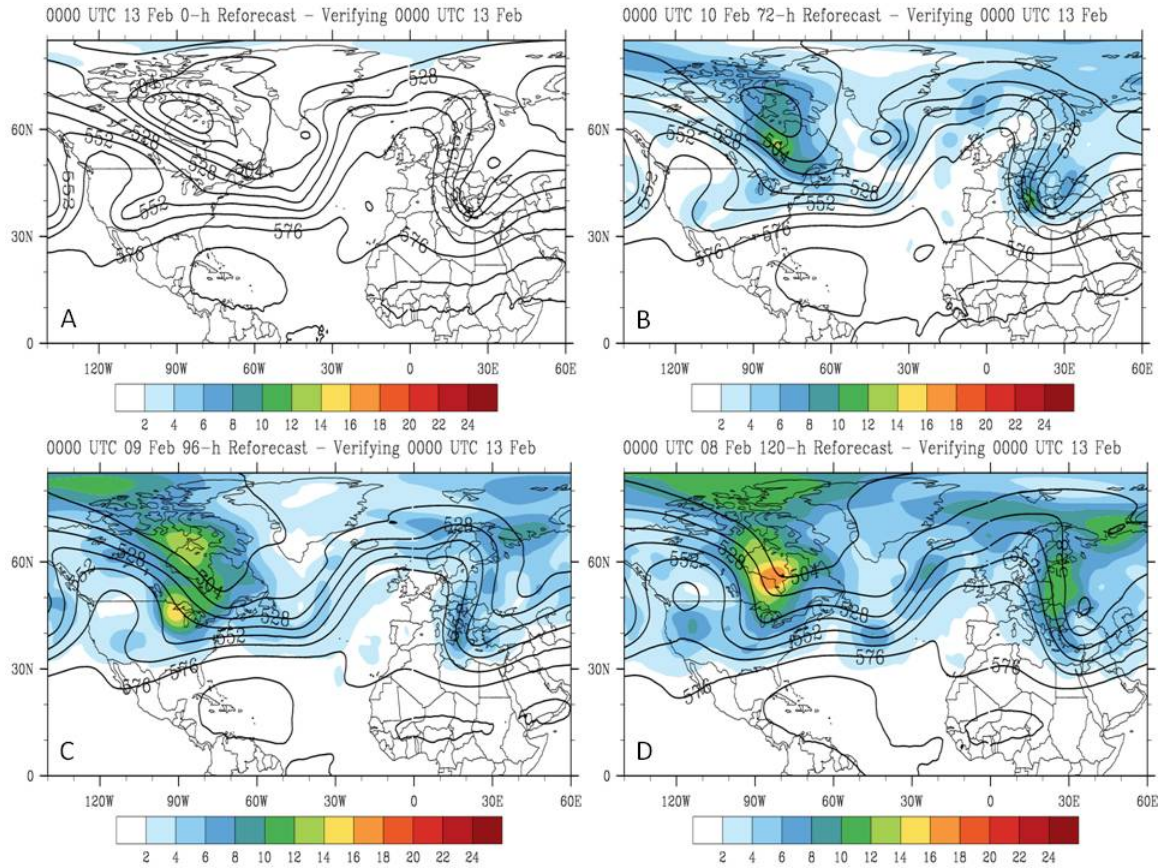


Figure 26. The 0000 UTC 13 February analyzed 500 hPa ensemble-mean heights, and the (b) 72-h, (c) 96-h, and (d) 120-h ensemble-mean forecasts of 500 hPa heights (black contours in dam). Shading represents standard deviation (m) about the ensemble.

The forecasts of SLP depict two regions of increased spread associated with the ridge-trough couplet. One region exists at the apex of the ridge, between Iceland and Greenland. The second region is over eastern Europe. Through the 96-h forecast (Figure 27c) the magnitudes of the spread in the ridge and trough east of the ridge increased at the same rate. Beyond 96-h, spread increased drastically over the entire region of northern Europe (Figures 27d, 28d, and 29d). Similar to the 500 hPa forecasts, the regions of greatest spread progresses downstream as the ridge develops (Figure 27).

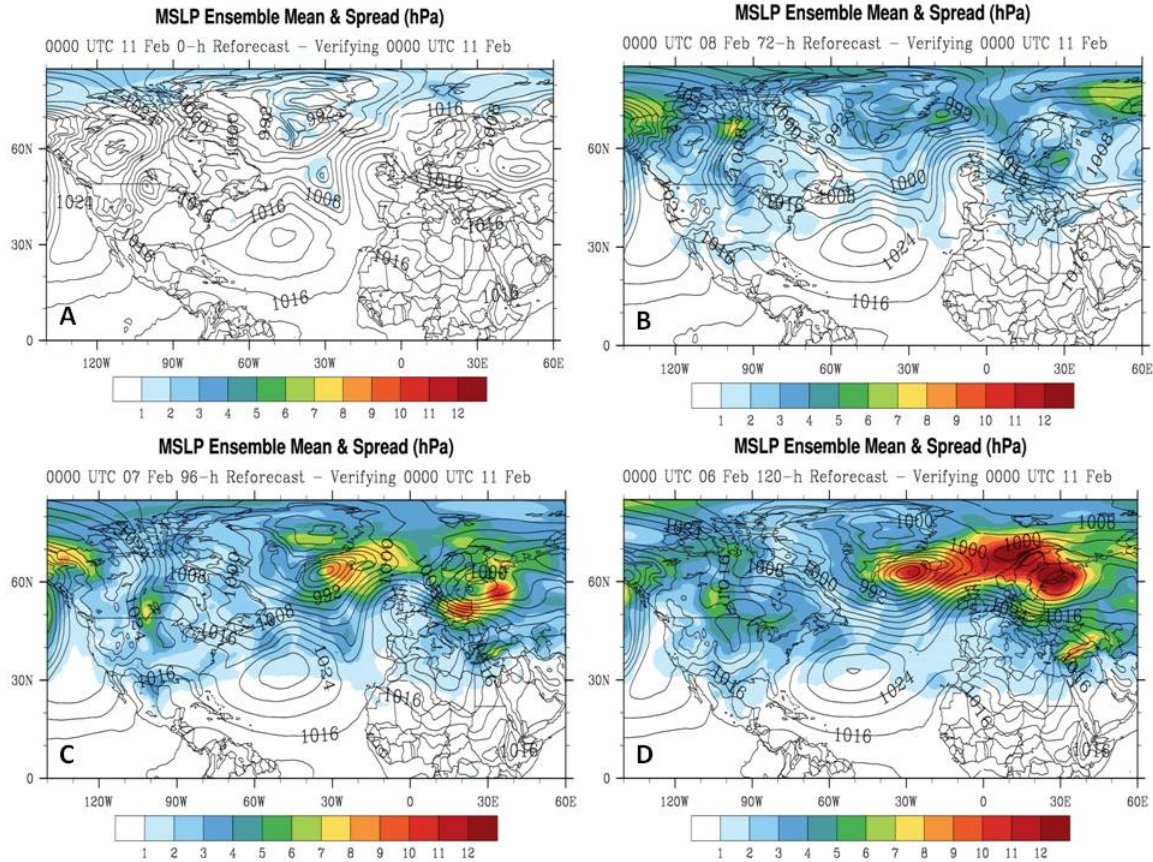


Figure 27. The 0000 UTC 11 February analyzed SLP ensemble-mean heights, and the (b) 72-h, (c) 96-h, and (d) 120-h ensemble-mean forecasts of SLP (black contours in hPa). Shading represents standard deviation (hPa) about the ensemble.

Ensemble forecasts of SLP that verify at 0000 UTC 12 February (Figure 28) define a slight shift in the pattern of uncertainty. Maximum spread among ensemble members is concentrated at high latitudes. Spread over the North Atlantic between Iceland and Greenland is reduced (Figure 28b–28d). However, spread over southeastern Europe remains large. At 120 h (Figure 28d), a separate maximum in spread occurs over the Aegean Sea. The pattern is similar to that of forecasts of 500 hPa that verify at 0000 UTC 12 February as the spread associated with troughing over southeastern Europe become larger than the spread over the upstream ridge (Figure 25).

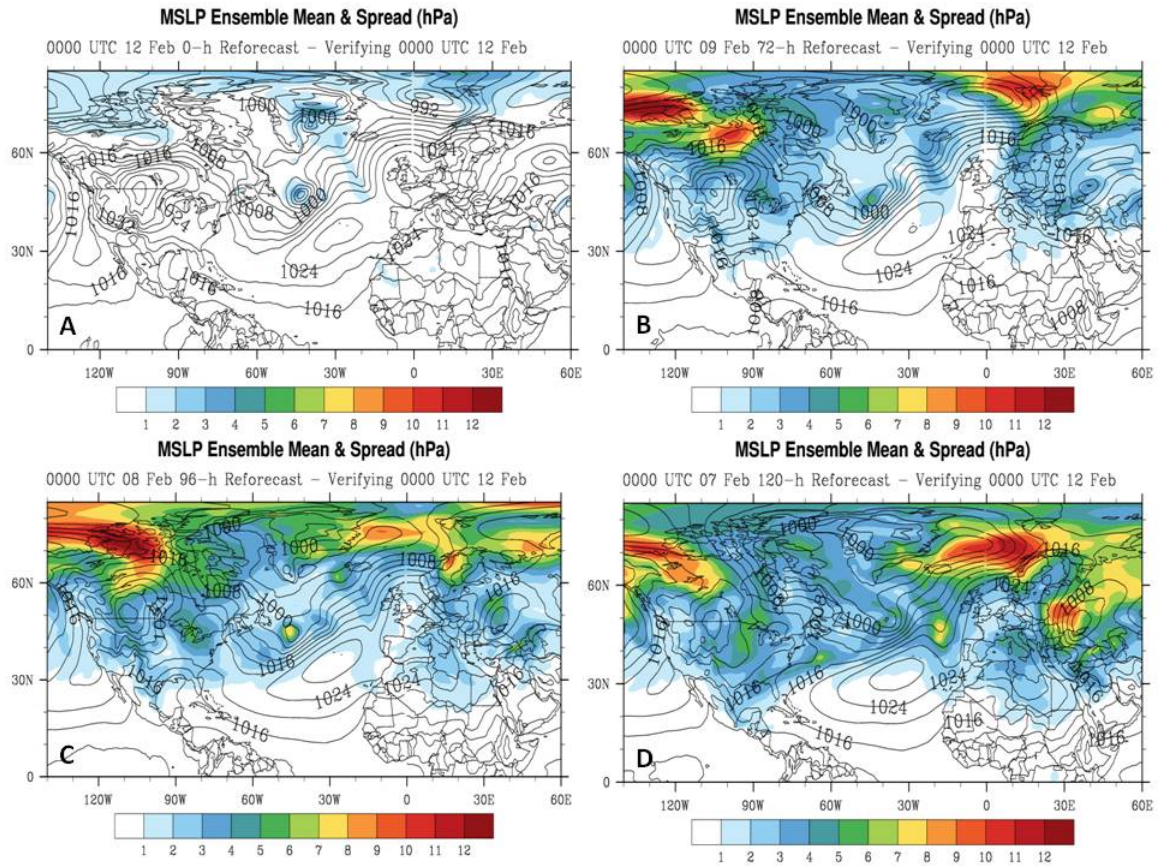


Figure 28. The 0000 UTC 12 February analyzed SLP ensemble-mean heights, and the (b) 72-h, (c) 96-h, and (d) 120-h ensemble-mean forecasts of SLP (black contours in hPa). Shading represents standard deviation (hPa) about the ensemble.

At the time of maximum thinning and equatorward extension of the trough (Figure 26), the uncertainty contained in ensemble forecasts of SLP has been reduced with respect to the ridge-trough couplet (Figure 29). Uncertainty in forecasts of SLP remains large at high latitudes and only a small region of moderate spread exists over southeastern Europe near 38°N 27°E. The region of uncertainty that is associated with the cyclone event over the eastern Mediterranean appears in the 72-h forecast (Figure 29b) that verifies at 0000 UTC 13 February. However, it does not increase in magnitude with increasing forecast interval.

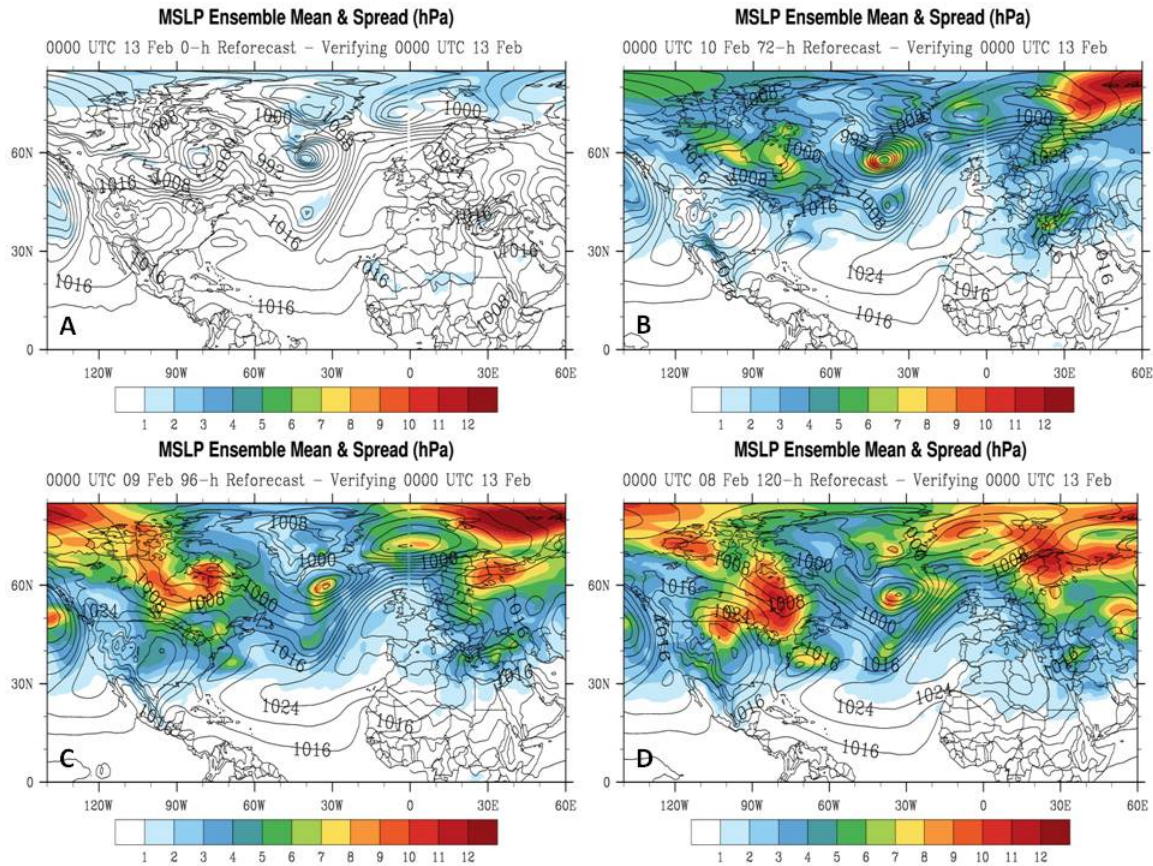


Figure 29. The 0000 UTC 13 February analyzed SLP ensemble-mean heights, and the (b) 72-h, (c) 96-h, and (d) 120-h ensemble-mean forecasts of SLP (black contours in hPa). Shading represents standard deviation (hPa) about the ensemble.

To summarize forecast uncertainty, as represented by ensemble forecasts of 500 hPa height and SLP, it is clear that the height forecast uncertainty appears initially to be associated with the ridge-building over the north Atlantic. Forecast uncertainty then increases downstream as the uncertainty in the ridge building decreases. Forecast uncertainty increases with increased forecast range until the time of the maximum cold surge. At this time, the forecast uncertainty becomes small and does not increase with increased forecast range.

To examine the predictability in greater detail, individual ensemble members were also examined. The forecasts of SLP and 500 hPa are examined using the 996 hPa contour and 540 dam height contour, respectively. The

forecasts of SLP are used to evaluate member performance for cyclones L1, L2, and L3, and the forecasts of 500 hPa are used to evaluate member performance for the North Atlantic ridge and eastern European trough. Examination of the individual members provides insight into the differences among the members that led to the spread depicted in the ensemble mean plots. Because forecast spread seems to propagate downstream, the series of three successive cyclones in the western Atlantic were examined first, the North Atlantic ridge was examined second, and the eastern European trough was examined last. It is hypothesized that ensemble members that accurately forecast the cyclones should subsequently accurately forecast the ridge and trough.

Although the determination of which ensemble member performed best is done by visual inspection, several criteria were used to rank the members. The location of the forecast features is examined, then the intensity of each forecast is examined. The member with the best position and intensity forecast was chosen as the best member of each forecast of L1, L2, L3, ridge, and trough. The best members for each forecast initialization time at verification times associated with L1, L2, L3, the trough, and ridge are listed in Table 1. Not all entries in Table 1 are discussed here. Rather, selected forecasts initiated at 0000 UTC 4 and 5 February are discussed to provide detail in the process by which the best forecast member was determined. These forecasts correspond to the second and third rows in Table 1.

Forecasts that verify at 0000 UTC 7 February, which was the time of cyclone, L1, were examined first. Because the spread among members is small in short-interval forecasts, the individual members are examined for 72-h forecasts and beyond. It is clear that forecasts of L1 that verify at 0000 UTC 7 February (Figures 30b, 30c) over forecast the intensity of L1. Based on the forecast intensity, member 6 performed best (Table 1) for the 72-h forecast initialized on 4 February (Figure 30b). Similar intensity and position forecast characteristics were evident in forecasts initiated at other times (Figures 30c).

For example, member 9 in the 96-h forecast initialized at 0000 UTC 3 February was determined to be best as the 996 hPa contour is most similar to the verifying contour.

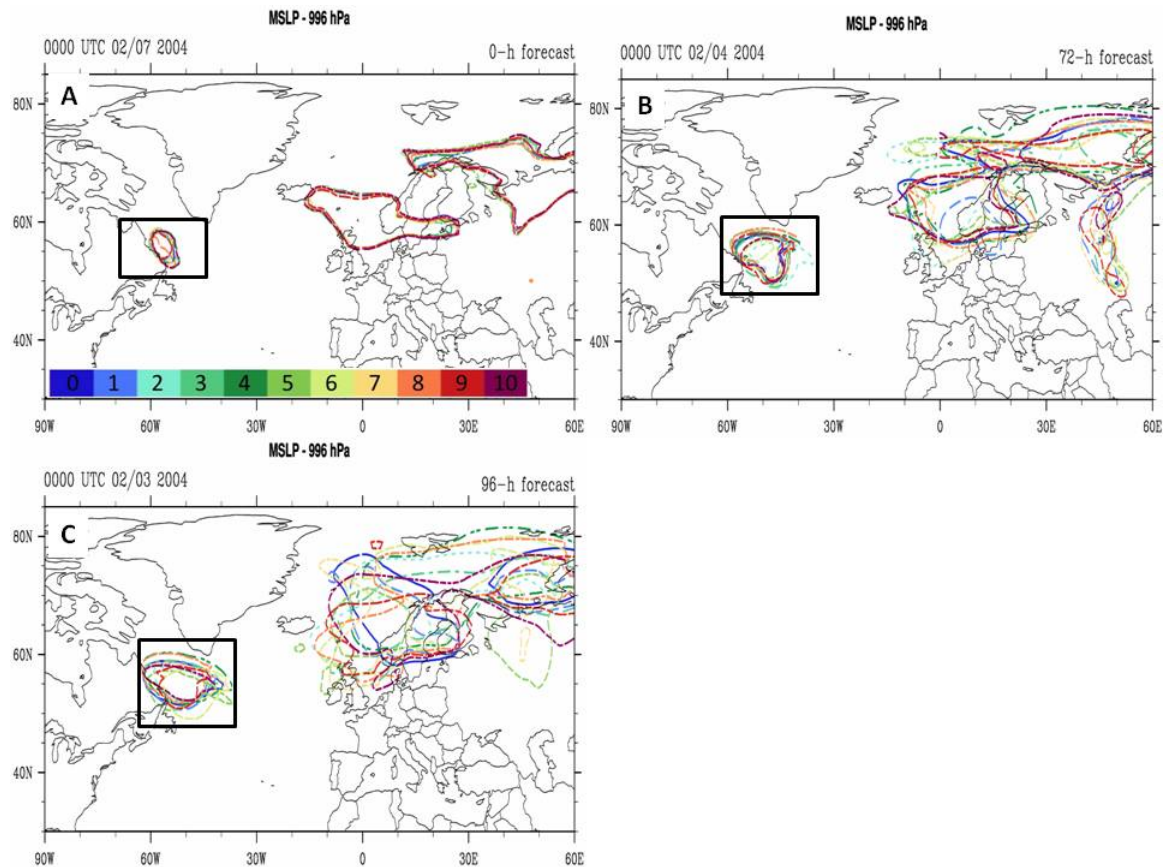


Figure 30. The 996 hPa contour for the ensemble members for the (a) analysis at 0000 UTC 7 February, the (b) 72-h forecast, and (c) 96-h forecast that verify at 0000 UTC 7 February. The black box defines the area of L1 over which the members are evaluated.

The time of 0000 UTC 9 February (Figure 31a) was used as the verification time for forecasts of cyclone L2. As with L1, forecast positions were generally accurate, but the forecast intensities of L2 were greater than the analysis. In the 120-h forecast initialized on 4 February (Figure 31b) member 5 is chosen to be the best as the 996 hPa contour encompasses less area than defined by other members, which indicates that the cyclone is weakest in member 5.

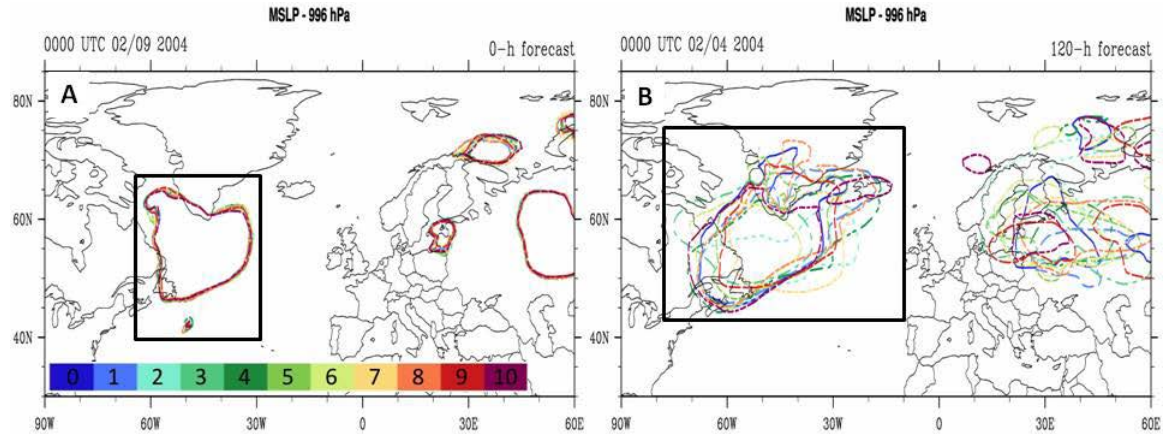


Figure 31. The 996 hPa contour for the ensemble members for the (a) analysis at 0000 UTC 9 February and the (b) 72-h forecast that verifies at 0000 UTC 9 February. The black box defines the area of L2 over which the members are evaluated

The time of 0000 UTC 10 February was used as the verification time for forecasts of cyclone L3 (Figure 32a). In the 144-h forecast initialized at 0000 UTC 4 February, member 5 performed best with respect to L3 (Figure 32b). This member also was the best 120-h forecast of L2 (Figure 31b). Therefore, the member that best forecast L2 also was the best forecast of L3 24-h later.

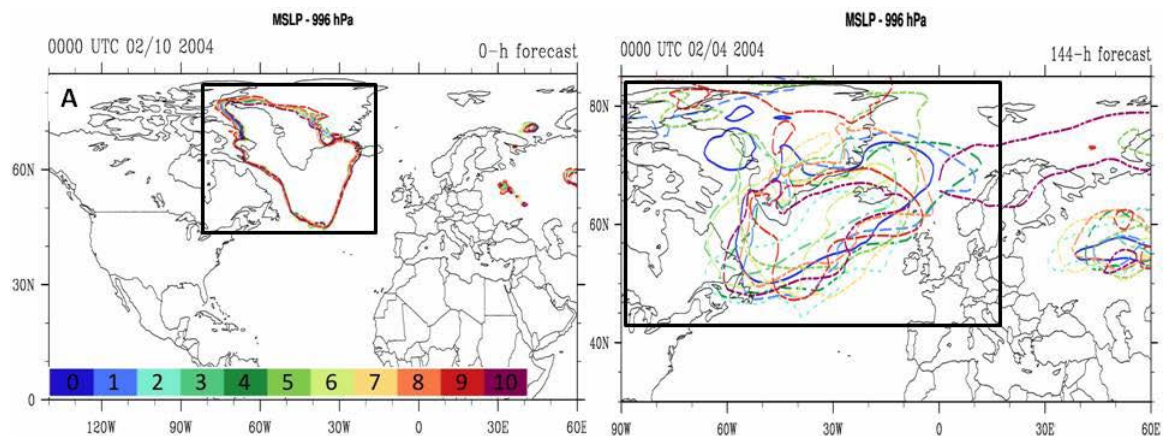


Figure 32. A comparison of the (a) 0000 UTC 10 February SLP analysis to the (b) 144-h forecast. The black box defines the area of L3 over which the members are evaluated.

The North Atlantic ridge is examined at the analysis time of 0000 UTC 11 February (Figure 33a). In the 168-h forecast initialized on 4 February, it is clear that member 6 contains the most accurate representation of the ridge (Figure 33b). Member 6 is the only ensemble member in which the 540 dam contour extended to Iceland (Figure 33b) as it does in the verifying analysis (Figure 33a). For the 144-h forecast that was initiated 0000 UTC 5 February, member 6 also performed best (Figure 33c). Again, member 6 was the only forecast member in which the 540 dam contour extended into Iceland as verified (Figure 33a).

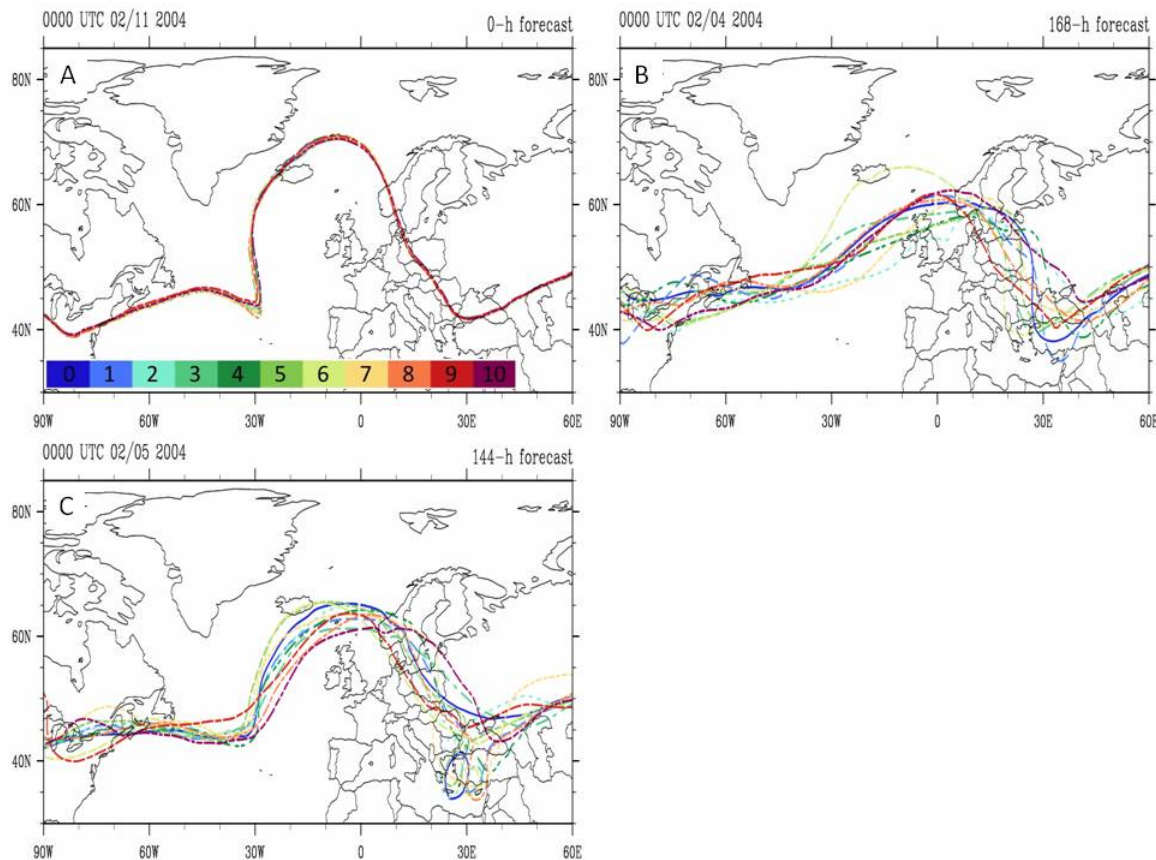


Figure 33. The 540 dam contour for the ensemble members for the (a) analysis at 0000 UTC 11 February, the (b) 168-h forecast initialized 0000 UTC 4 February, and the (c) 144-h forecast initialized 5 February that verify at 0000 UTC 11 February.

The time used to examine the eastern European trough was defined to be 0000 UTC 13 February (Figure 34a). From the 192-h forecast initialized 0000

UTC 5 February, it is clear that the best member was again member 6 (Figure 34b). Member 6 forecasted a strong anticyclonic wavebreak with a thinning trough over eastern Europe.

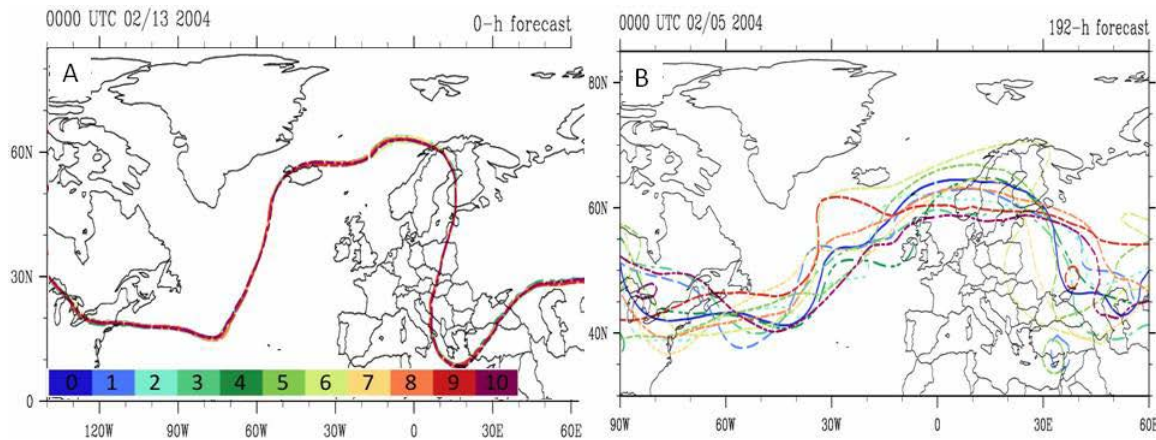


Figure 34. The 540 dam contour for the ensemble members for the (a) analysis at 0000 UTC 13 February and the (b) 192-h forecast initialized 0000 UTC 5 February that verify at 0000 UTC 13 February.

Although it is not possible to address every entry in Table 1, it is clear that identification of best-performing ensemble members tends to confirm the hypothesis that accurate forecasts of the ridge favored accurate forecasts of the downstream trough.

In four of six cases in which there are verifying forecasts of the ridge-trough couplet (i.e., initial times of 5–10 February in Table 1), the ensemble member that forecast the North Atlantic ridge best also forecast the eastern European trough best. Additionally, this consistency among ensemble members occurred for both extended-range forecasts (i.e., initial time of 5 February) and short-range forecasts (i.e., initial time of 10 February).

A measure of chance likelihood for the same member to be the most accurate for two verifying times is considered. Each of the 11 members is considered to be best at any verifying time with equal probability. It is also assumed that a member that is best at one verifying time is independent of the

member that is best at an adjacent verifying time. The conditional probability of the same member being best for two verifying times is then $(1/11)^2$. For the forecasts of the ridge-trough couple listed in Table 1, the frequency at which the best forecast member for the trough is much higher than the probability of having the same member being the best forecast due to chance.

There are no member forecasts that are best for all three precursor cyclones, L1, L2, and L3 (Table 1). There are two instances in which the same member provides the best forecasts for L2 and L3. These occur for the five-day and six-day forecasts initiated at 0000 UTC 4 February and the two-day and three-day forecasts initiated at 0000 UTC 7 February. However, these members do not exhibit the best forecasts for the North Atlantic ridge.

Only the two-day and three-day forecasts initiated at 0000 UTC 8 February have a member that provided the best forecast of L3 and a best forecast for the ensuing North Atlantic ridge. However, there are two sets of forecasts, initiated on 0000 UTC 4 and 5 February, in which the member that had the most accurate forecast of L1 also had the most accurate forecast for the North Atlantic ridge. For the case of the forecast initiated on 5 February, the same member also had the best representation of the eastern European trough.

In summary, the members listed in Table 1 indicate that accurate forecast of the North Atlantic ridge did lead to an increased likelihood of an accurate forecast of the ensuing eastern European trough. However, there is less of a connection to forecasts of the precursor cyclones L1, L2, and L3. Although it is clear from the analysis in Section 3.1 that the WCBs associated with the successive cyclone contributed to the building of the North Atlantic ridge, this process was not consistently related to the downstream evolution as defined by members of the ensemble forecast system.

	L1 7 Feb	L2 9 Feb	L3 10 Feb	Ridge 11 Feb	Trough 13 Feb
3 Feb	9	9	2	2	N/A
4 Feb	6	5	5	6	N/A
5 Feb	6	2	10	6	6
6 Feb	N/A	2	7	2	2
7 Feb	N/A	8	8	2	6
8 Feb	N/A	N/A	7	7	8
9 Feb	N/A	N/A	4	1	1
10 Feb	N/A	N/A	N/A	9	9

Table 1. A list of which ensemble members best forecast the synoptic features for forecasts initialized 3–10 February. Shading in a row defines a member providing the best forecast for a given feature.

In summary, examination of individual ensemble members supported the hypothesis that accurate forecasts of the North Atlantic ridge lead to accurate forecasts of the downstream trough over eastern Europe. However, there was no statistical linkage identified between forecast accuracy of the precursor cyclones and that of the North Atlantic ridge. Although the WCBs of each successive cyclone clearly contributed to the ridge-building event, this process was not consistently represented in ensemble forecasts. Therefore predictability for the cold surge event only extended back to the wavebreaking process and not the forcing of the high-amplitude ridge, which may be highly dependent on diabatic processes. A caveat to the interpretation of Table 1 is that a rather small ensemble is used to perform a limited statistical evaluation of the sequence of events that lead to the cold surge over Crete.

THIS PAGE INTENTIONALLY LEFT BLANK

V. CONCLUSIONS AND RECOMMENDATIONS

On 13 February 2004, an extreme cold surge resulted in significant snow fall over Naval Support Activity Souda Bay. The extreme nature of the cold surge led to severe difficulty in forecasting the event. As a result of that forecast difficulty, NSA Souda Bay was not prepared for the ensuing snowfall and base operations were delayed, and the airfield was closed until Navy personnel could clear the flight line of snow.

A. SYNOPTIC DEVELOPMENT

In this thesis, the development of the cold surge event is examined relative to a sequence of precursor synoptic-scale events. These events include a sequence of cyclones that occurred over the western Atlantic beginning seven days prior to the cold surge. The WCB from the series of three extratropical cyclones worked to build a highly-amplified ridge. The cold surge was then the result of an anticyclonic wavebreak that developed in response to the extreme ridge-building event over the North Atlantic southeast of an amplified transient synoptic-scale ridge.

The physical linkage between the three cyclones and the highly amplified North Atlantic ridge was determined to be repeated forcing by the WCBs associated with each cyclone. Diabatic processes associated with the WCBs contributed to negative PV tendencies at upper-levels as the mid-tropospheric ridge amplified.

Following the time of maximum amplitude of the North Atlantic ridge, a downstream trough developed as a LC1 anticyclonic wavebreak. In response to horizontal anticyclonic shear, the North Atlantic ridge acquired a large northeast to southwest orientation. A deepening downstream trough extended to the southwest over eastern Europe. Throughout the two days of the wavebreaking event, the trough thinned and extended to the Mediterranean and Aegean Seas.

The deep trough was associated with a high-amplitude tropopause fold in which stratospheric air extended downward to 700 hPa.

At the time of maximum intensity of the trough, the 300 hPa heights associated with the deep eastern European trough were four standard deviations below the climatological long-term mean height. Likewise, at the time of peak intensity of the ridge, the 300 hPa were two standard deviations above the mean.

B. PREDICTABILITY

The predictability of the cold surge over Crete was examined using an ensemble forecast system that contained 10 members and one control. In this case, predictability was defined by the spread among ensemble members and by consistency with forecast accuracy among individual ensemble members.

Spread among ensemble members was consistently located at the apex of the North Atlantic ridge and near the base of the eastern European trough. For daily forecasts that were of extended ranges, the spread associated with the ridge was larger than that in the trough. However, the ridge amplified and valid forecast ranges shortened. The amplitude of spread on the ridge decreased while amplitude on the trough increased. Therefore, forecast uncertainty moved downstream as the ridge-trough couplet developed.

C. RECOMMENDATIONS

It is recommended that forecasters, especially in winter months and at high latitudes, examine precursor events several days before a forecast valid time and well upstream of features of interest. Examining highly amplified, synoptic-scale, patterns provides significant insight into expected downstream conditions. Additionally, when using ensemble products, forecasters should understand that the ensemble mean for highly anomalous cases will likely not provide an accurate portrayal of future conditions. Finally, diabatic forcing of the

high-amplitude ridge may forecast skill of high-impact weather events. Accordingly, forecasters should note that regions of strong diabatic forcing may be sources of high forecast uncertainty and error.

THIS PAGE INTENTIONALLY LEFT BLANK

LIST OF REFERENCES

- Altenhoff, A., O. Martius, M. Croci-Maspoli, C. Schwierz, and H.C. Davies, 2008: Linkage of atmospheric blocks and synoptic-scale Rossby waves: a climatological analysis. *Tellus*, **60A**, 1053–1603.
- Carlson, T. N., 1980: Airflow through midlatitude cyclones and comma cloud pattern. *Mon. Wea. Rev.*, **108**, 1498–1509.
- Danielsen, C. A. and D. Hipskind, 1980: Stratospheric-tropospheric exchange at polar latitudes in summer. *Journal of Geophysical Research*, **85**, 393–400.
- Davis, C. A. and K.A. Emanuel, 1991: Potential vorticity diagnostic of cyclogenesis. *Mon. Wea. Rev.* **119**, 1929–1953.
- Eckhardt, S., A. Stohl, H. Wernli, P. James, C. Forster, and N. Spichtinger, 2004: A 15-year climatology of warm conveyor belts. *J. Climate*. **17**, 218–237.
- Hamill, T.M., R. Hagedorn, and J.S. Whitaker, 2008: Probabilistic forecast calibration using ECMWF and GFS ensemble reforecasts. Part II: Precipitation. *Mon. Wea. Rev.*, **136**, 2620–2632.
- Hamill, T.M, and co-authors, 2013: NOAA's second-generation global medium-range ensemble reforecast data set. (In Press)
- Hart, R.E., and R.H. Grumm, 2001: Using Normalized Climatological Anomalies to Rank Synoptic-Scale Events Objectively. *Mon. Wea. Rev.*, **129**, 2624–2442.
- Hoskins, B., M. McIntyre, and A. Robertson, 1985: On the use of significance of isentropic potential vorticity maps. *Quarterly Journal Roy. Meteor. Society*, **111**, 877–946.
- Joos, H., and H. Wernli, 2012: Influence of microphysical processes on the potential vorticity development in a warm conveyor belt: a case-study with the limited-area model COSMO. *Quarterly Journal of the Roy. Meteor. Society*, **138**, 407–418.
- Kalnay, E., 2006: *Atmospheric Modeling, Data Assimilation, and Predictability*. Cambridge University Press, 341 pp.
- Morgan, M.C., and J.W. Nielson-Gammon, 1997: Using tropopause maps to diagnose midlatitude weather systems. *Mon. Wea. Rev.*, **126**, 2555–2579.
- Pettersen, S., and S.J. Smebye, 1971: On the development of extratropical cyclones. *Quarterly Journal of the Roy. Meteor. Society*, **97**, 457–482.

- Pfahl, S. and H. Wernli, 2012: Quantifying the relevance of atmospheric blocking for co-located temperature extremes in the Northern Hemisphere on (sub-) daily time scales. *Geophysical Research Letters*, **39**.
- Pomeroy, H.R., and A.J. Thorpe, 2000: The evolution and dynamical role of reduced upper-tropospheric potential vorticity in Intensive Observing Period 1 of FASTEX. *Mon. Wea. Rev.*, **128**, 1817–1834.
- Saha, S., and co-authors, 2010: The NCEP Climate Forecast System Reanalysis. *Bull. Amer. Meteor. Soc.*, **91**, 1015–1057.
- Simmons, A.J., and B.J. Hoskins, 1980: Barotropic influences on the growth and decay of nonlinear baroclinic wave. *J. Atmos. Sci.*, **37**, 1679–1684.
- Stoelinga, M.T., 1996: A potential vorticity-based study of the role of diabatic heating and friction in a numerically simulation baroclinic cyclone. *Mon. Wea. Rev.*, **124**, 849–874.
- Thorncroft, C. D., B.J. Hoskins, and M.E.McIntyre, 1993: Two Paradigms of baroclinic-wave life-cycle behaviour. *Quarterly Journal of the Roy. Meteor. Society*, **119**, 17–55.
- Trigo, I., G. Bigg, and T. Davies, 2002: Climatology of cyclogenesis mechanisms in the Mediterranean. *Mon. Wea. Rev.*, **130**, 549–569.

INITIAL DISTRIBUTION LIST

1. Defense Technical Information Center
Ft. Belvoir, Virginia
2. Dudley Knox Library
Naval Postgraduate School
Monterey, California